Investigating the heat-treatment process for 316L alloy powders with the application in binder jetting metal additive manufacturing

by

Ali Zardoshtian

A thesis

presented to the University of Waterloo

in fulfillment of the

thesis requirement for the degree of

Master of Applied Science

in

Mechanical & Mechatronics Engineering

Waterloo, Ontario, Canada, 2020

AUTHOR'S DECLARATION

I hereby declare that I am the sole author of this thesis. This is a true copy of the thesis, including any required final revisions, as accepted by my examiners.

I understand that my thesis may be made electronically available to the public.

Abstract

Metal binder jetting (BJ) is a manufacturing process which involves the deposition of metal powder and an adhesive liquid binder layer-by-layer to fabricate metal parts. BJ as-printed parts are in essence loose particles bound together and must be sintered at high temperatures to create dense structures. It is catching industry's attention since it is fast, cost-effective and enables fabrication of more complex geometries in comparison to other manufacturing processes such as casting and conventional powder metallurgy. However, BJ is a relatively new technology and requires more -pre and -post process development to enhance its applicability for the industry.

One of the major concerns in BJ technology is the porosity left after sintering the green parts. This strongly depends on the sinterability of the metal powder. Therefore, this thesis focuses to evaluate the effect of powder particle size distribution (PSD), green density of printed samples and thermal treatment on the sinterability of 316L powders. Three different atomized 316L powders with different PSD are selected for this thesis including a unimodal fine powder and two bimodal coarse powders. Prior to starting sintering experiments, thermal analysis of metal powders and polymeric binder is conducted with differential scanning calorimetry and thermal gravimetric analysis, respectively. The decomposition temperature of the binder and the solidus temperatures of the powders were found out to create a sintering schedule which can remove the binder effectively and guarantee sub-solidus sintering.

An analytical model for the densification was used to construct the master sintering curve (MSC) to compare the effect of PSD and green density on the consolidation. It was found out that the apparent activation energy of sintering was not affected by the PSD and the green density. The microstructural analysis with SEM showed that sintering occurred through solid stated diffusions in austenite and δ-ferrite. The kinetics of sintering changed slightly with PSD. Powder with a fine unimodal PSD required less work to activate sintering and had a faster sintering rate which lead to the highest density (95%). Fine bimodal powder had also similar kinetics while coarses bimodal powder required more work to initiate the sintering. A slower densification rate resulted in lower relative density (92%).

The green density had more profound effect on the sinterability of powders. The work required to trigger sintering was increased by 17.5 % when the green density was reduced from 65% to

53%. This was much higher than what was observed when the PSD was modified. As a reference, the difference in the onset of sintering for the UMC and BMC is only 12.2%. Decreasing the green density also reduced the densification rate and leads to a much lower final density.

The final microstructure was analyzed using scanning electron microscope equipped with an Energy-dispersive detector. Detrimental sigma-phase was identified in the sintering 316l microstructure. A solutionizing post-heat treatment has been developed to re-solution the sigma-phase into ferrite.

The work done on the powder properties and green density will be used as the basis for further studies on densification. The BJ process development will be undertaken by optimizing the printing parameters. Sintering schedules will be revisited to reduce the volume fraction of detrimental σ-phase.

Acknowledgments

First and foremost, I would like to thank my supervisor, Dr. Etienne Martin for the opportunity he provided me along with his continuous support throughout my master studies. I gained a lot of experience by working under his supervision. Second, I want to thank my thesis reviewers Prof. Kaan Inal and Prof. Mustafa Yavuz for the time they dedicated to reading my thesis. Also, special thanks to the postdocs of our group, Dr. Rasim Batmaz and Dr.Waqas Muhamad for their collaboration on the experiments and reviewing my thesis.

I appreciate the collaboration that I received from people at the Multi-Scale Additive Manufacturing laboratory, especially Dr. Ehsan Marzban for his kind assistance with some experiments.

I have to thank my amazing group members Aprateem, Reza, and Sol who I have had a great time and fun with them.

Many thanks to my friends in the department of mechanical engineering, East Campus 4 building, and others in Iran; Maedeh, Amin, Abozar, Mehdi, Milad, Pedram, Reza, Alireza, Salman, Shahriar, Moslem, Chi-Hsiang, Hamed, Issa and many other people who mentally supported me and brought a cheerful atmosphere to my life during my master studies.

Last but not least, I will always be grateful to my family, particularly to my mother for her continuous support, endless love, and huge encouragement. Thank you mom from the other side of the world.

Dedication

To the soul of my beloved father whose great memories will always stay in my mind, and the heart of my devoted mother whose endless support has never left my side.

Table of Contents

List of Figures

List of Tables

Chapter 1
Introduction

Additive manufacturing (AM), also known as 3D printing, is gaining increased attention and interest due to the substantial increase in the demand for high performance materials with added functionalities (such as internal cooling channels or internal lattice structures, which are difficult to fabricate with conventional manufacturing processes) and increased complexities in geometrical design. ***Binder Jetting (BJ)*** is an AM processes originally developed at Massachusetts Institute of Technology (MIT) in the early 1990s. BJ processes print a liquid binder into a powder bed to fabricate a part. Layers of material are then bonded to form an object. Once a layer is printed and thermally dried/cured, a new layer of powder is recoated on top of the previous layer which is then printed and stitched to the previous layer by the jetted binder. The layer-by-layer process is repeated to create the complete green part. Once de-powdered, the green part is placed in a furnace to burn off the binder and to sinter the powder particles together to obtain final density and strength. BJ processes has many advantages relative to other AM processes. Because it is a room-temperature process, residual stresses imposed by large thermal gradient and cracking mechanisms observed in SLM are avoided. Binder Jetting is an inherently scalable and cost-effective technology, which has been demonstrated in many commercial systems.

1.1 Motivation

As stainless steel powders are widely used powders in BJ and MIM, understanding the densification behaviors of stainless steel powders is of great importance and interest to successful sintering processes. Within stainless steel families, 316L stainless steel has excellent mechanical properties along with high corrosion resistance, oxidation resistance, high heat resistance, and good weldability. In this regard, 316L stainless steel have played an important role in powder metallurgy research and industrial applications such as pharmaceuticals, architectural and medical applications. There has been a limited amount of work on the effects of particle size and particle size distribution on the mouldability and sinterability of MIM and BJ powders. The focus of the most work available is on the influence of particle shape and powder

loading on the flowability of MIM feedstock and hence the final mechanical properties of the sintered parts. To date, the literature lacks a systematic study to analytically and experimentally identify the linkages between the PSD, initial green density, post processing parameters and the final density of the BJ-manufactured parts. In this work, we use analytical tools to evaluate the effect of PSD and green density on the sinterability of 316L powder.

1.2 Objectives

The scope of this thesis focuses on investigating the powder characteristics for BJ process. The objectives can be summarized as follows:

1. Find the best PSD for the BJ process in terms of sinterability and flowability. The best PSD should have a proper flowability as well as being able to pack well to reach high green densities and subsequently obtain high final density after sintering.
2. Define an optimum heat-treatment profile for BJ products. The heat-treatment consists of three major stages; de-binding, sintering, and post sintering heat treatment. Debinding is supposed to remove the binder from the green sample leaving a minimum amount of residue. Sintering is defined concerning the solid-state sintering regime and to reach maximum density. And finally, a post sintering heat-treatment is defined to lead a microstructure without detrimental phase(s).
3. Establish a sintering model in order to predict the final part density and observe the effect of PSD and green density on sintering behavior. For that purpose, an analytical model based on the master sintering curve (MSC) is developed. The MSC is an empirical tool, that was adopted by powder metallurgy before, enables the comparison between each variable which affects the sinterability of BJ parts.

1.3 Thesis Structure

This thesis consists of five chapters in total. As stated above, the first chapter gives away the introduction on AM and BJ as well as the motivation. Chapter 2 comprehensively talks about the background and literature review of BJ, the alloy that is used, sintering, and the analytical model. Chapter 3 covers the methodology and the experiments used to evaluate powder characteristics and density measurement as well as the designed heat treatment profile for the samples. The fourth chapter presents the results and discussions over the experimental data as well as the ones

from the MSC. Finally, chapter 5 brings the conclusions of this piece of work and suggests the potential future works based on the efforts that were done and summarized in this thesis.

Chapter 2

Background & Literature Review

2.1 Introduction to Binder Jetting technology

The additive manufacturing (AM) technology which is also called Three-dimensional printing (3-D Printing) and Rapid Prototyping (RP), was introduced first in the 1980s and since then it has been catching more attention mainly due to manufacturing complex geometries directly from computer-aided design (CAD) files with a noticeable lower rate of the cost than other conventional manufacturing processes like casting and forging. [1–5]. Basically, in an AM process, parts are built by selectively adding materials layer-by-layer from three-dimensional (3D) models. To date, additive manufactured parts from a wide range of materials including metals, ceramics, polymers, sand, and glass have been introduced to many high-tech industries, such as biomedical, aerospace, and automotive. Based on American Society for Testing and Materials (ASTM) Standards, AM processes are categorized into seven process types: material jetting, vat photopolymerization, sheet lamination, direct energy deposition (DED), powder bed fusion (PBF), material extrusion, and binder jetting (BJ) which is getting more attention nowadays from the industry thanks to its applicability for an unlimited range of materials in room temperature and atmosphere [5-9].

2.1.1 Binder Jetting Process Description

Binder jetting (BJ) is a subgroup of additive manufacturing which is a very useful technique for rapid prototyping and manufacturing of metallic, composite and ceramic materials. This method of additive manufacturing was first time invented by Michal J. Cima and his colleagues at Massachusetts Institute of Technology (MIT) in 1993 then brought to the industry by Z Corporation in 1994, Voxeljet in 2005, ExOne in 2010 and Desktop Metal in 2017 [5, 8]. Dislike the other powder bed AM technologies that input laser or electron beam to fuse powder particles, no heat source or fusion is needed during the BJ process although all printed parts need to go under a sort of post-processing. In this method of additive manufacturing, a liquid binder

selectively pours on the powder bed to join the powder particles layer-by-layer in order to form the designed part from 3D CAD file [10-12]. The printing process is shown in Figure 2.1, it starts with spreading a thin layer of powder by the leveling roller from powder stock and forms the powder bed on the build platform. Then the printhead jets liquid binder onto surface areas corresponding to 2D layers taken from the 3D CAD file leads to bounding powder particles together in the selected areas. Once the printing process on one layer is finished, the build platform goes down to a certain height and a new layer of powders is spread on the finished layer. This procedure is repeated until the whole designed part is printed. [13,14]

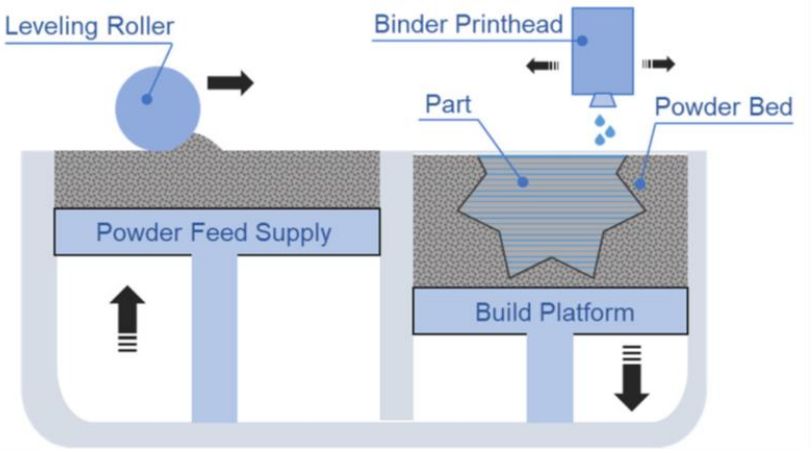

Figure 2.1 The schematic illustration of the printing step in BJ manufacturing process [13]

As previously stated, BJ is an AM method that selectively pours adhesive binder onto the surface of a thin layer of powder which leads to the construction of a designed part via layer-by-layer printing of a 3D CAD model. Recently, BJ has been getting more attention from the industry as this process does not use a powerful source of energy for construction, it became an economical method for manufacturing. Besides, BJ is a fast method for material deposition and eliminates some sub-processes that exist in conventional manufacturing [15]. Dislike other metal AM processes such as SLM and DED, in BJ the printing process is detached from the consolidating process. Thus, in comparison with other AM methods, the printing process in BJ is a simple step that has more freedom to manipulate its parameters for shape optimization regardless of final part properties yet some of the process parameters affect density and strength of finished parts. In the past, the main application of BJ technology was for fabricating sand molds and cores for the metal casting industry, however, it has been facing a transition to get used as the main process

method and the high productivity machines has been introduced for this technology in the last 5 years [17]. Since BJ is a sinter-based technology, it has a very well-known background of knowledge established in powder metallurgy, which gives engineers a good sight to find process issues and tackle them. Nevertheless, fabricating parts with the same densities and mechanical properties as those in conventional powder metallurgy (PM) processes is a challenge in the BJ process. [16]

Binder Jetting process chain

BJ process chain is shown in Figure 2.2 which basically consists of five steps: printing, curing, de-powdering, debinding & sintering, and post sintering. Once the printing procedure is finished, the printed part which is also called as "green part", first goes under "curing" process which heats the part to around 200°C and activates the binder system in order to reinforce the green part by polymerization, cross-linking, and solvent evaporation. After the curing process, the green part is not loose anymore and is ready for coming out of the powder bed in the process called de-powdering. Subsequently, the green part goes for the debinding process during which the binder is removed by burning out or thermal decomposition in a specific gas atmosphere. Based on the binder composition the temperature range for this process is between 300 °C to 800 °C. Following the debinding is the sintering step in which the part is heated up to a relatively high temperature to achieve a high density and strength by diffusion between the powder particles in a specific atmosphere. Finally, based on the application some optional techniques such as hot isostatic pressing (HIP) and infiltration may be implemented to modify gran size and a further increase in the sintered density to reach better mechanical properties. [14]

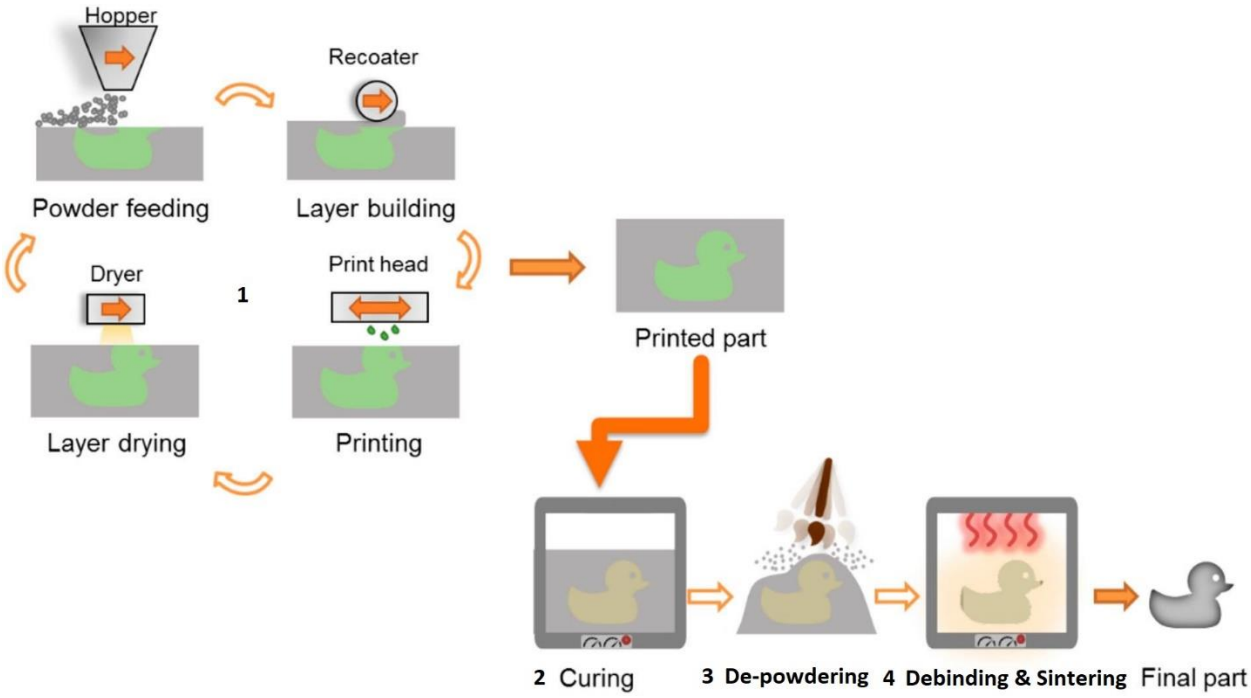

Figure 2.2 Binder Jetting additive manufacturing process chain from loose powders to the final part [16]

It is worth to mention the above steps were taken from ExOne binder jetting approach and there are some variations between different BJ machines such as powder deposition while some machines use a hopper to spread powder on the build platform, some other machines rely on piston feed mechanism to supply a new layer of powder. Moreover, the binder system which is used in different machines are different, and the curing step is designed based on the binder and even for some is not needed. Some BJ machines use organic binders and some of them use solid binders in the powder bed to increase the efficiency of the liquid binder [18].

The advantages of Binder Jetting technology

Generally, AM technologies have many advantages while the most important one can be named as their ability to fabricate complex geometries with any applicable material. Among all the AM technologies, BJ has some superiorities over other methods that have made it desirable nowadays. Unlike PBF and DED processes that apply laser or electron beam to fuse metal powders during printing in an inert atmosphere or vacuum, the printing step in BJ works at room atmosphere and temperature, which makes it applicable for heat-sensitive materials. [6,13]

Besides, because of local and rapid heating and cooling, nonuniform microstructure and residual stresses are common in PBF and DED products, on the other hand, thanks to the controllable sintering parameters, there is no residual stress nor nonuniform microstructure in BJ parts. [13]. Moreover, the need for support structure is eliminated in this process as the surrounding powders adequately can support the printing geometry in the powder bed [5,9] Untouched powders can be reused in the powder bed for the printing of next samples [11]. Based on what has been mentioned so far, BJ can be named as one of the most economical manufacturing, particularly AM techniques. Besides, recently BJ has been implemented into the manufacturing of automotive and heavy equipment. Table 2.1 briefly presents the companies that are using BJ technology and its field of application. [5,9,11,19].

The drawbacks of Binder Jetting technology

Generally speaking, binder jetting printed parts contain low initial packing densities which is usually around 50–60% of the theoretical density because of the lack of compressing forces in the printing step [16]. As pores in a porous part are the source of stress concentration, they easily lead to crack propagation. So, porosity elimination in the printed part is vital to achieving a solid figure which has reasonable mechanical properties [20]. On the other hand, obtaining high densities is always associating with a large amount of shrinkage during sintering which noticeably affects the dimensional accuracy. [10,11]. Therefore, controlling the shrinkage to achieve an accurate distortion-free geometry is another challenge in BJ productions. [13]

Table 2.1 MIT licensees for BJ [21]

Companies	Field of application
3D Systems (formerly Z corporation)	Rapid prototyping and concept modeling
Integra Lifesciences holding corporation	Production of time-release drug-delivery devices
TDK	Production of ceramic components for electronic application
CeraNova Corporation	Porous ceramic filters production
Soligen Inc.	Production of ceramic molds for metal casting
Voxeljet	Production of ceramic shells for investment casting
ExOne	Metallic parts and tooling, sand molds for casting
Viridis3D LLC	Fabrication of sand molds for metal casting

2.1.2 Binder Jetting General Variables

In general, the quality of a finished part produced via BJ has directly impacted by the whole process variables. Despite many advantages that BJ method has, in order to become competitive with conventional manufacturing methods in terms of quality of fabricated parts some weaknesses should be tackled or diminished such as porosity, weak mechanical properties, dimensional inaccuracy, and bad surface quality. Therefore, the BJ key parameters should be optimized to reach a desirable part. Studies on these process variables in which the following section discusses them can be categorized into pre-process, in-process, and post-process parameters [10,20]

2.1.2.1 Binder Jetting Pre-Process Parameters

Powders

Powder properties are the most impactful parameter among pre-process parameters [5]. Flowability, tap density, particle size and their distribution, and the morphology of powder particles can be named as major factors influencing the processability and quality of BJ manufactured part in terms of mechanical properties and physical features. The Flowability of a powder is the first feature that should be considered in material selection for the process which critically affects spreadability. As a powder bed AM technology, BJ requires a powder material with perfect spreadability. Powders with weak flowability, can not be spread smoothly and uniformly onto the bed and lead to detrimental defects in part structure through the printing step[12,22]. The tap density of powders has a direct effect on green density since there is no noticeable compacting force during powder deposition into the powder bed. Subsequently, green density influences the sintering behavior and final density of parts. [22].

Powder particle size and its size distribution (PSD) is another factor by which sinterability, flowability, wettability with the binder, surface roughness, and the part's dimensional accuracy are directly or indirectly affected [3,23,24, 26]. In BJ, size of the powders lies within a range of 0.2–200 μm [5] while powders with large particles have suitable flowability due to low interparticle friction and weak van der Waals forces, small particle size powders have better sinterability and powder-binder reactivity thanks to higher surface area per volume unit [12,27,28]. The weak flowability of fine powders can be modified by increasing the median particle size [23].

Generally, powders with too small particle size agglomerate because of the electrostatic forces between particles [11, 29] which results in the creation of large voids and weakens binder penetration in the powder bed. Besides, they have poor wettability because of a large angle of contact and agglomeration. Thus, using fine powder usually leads to detrimental defects in the printing step. [22,23,30] On the other hand, implementing bimodal powder size which is a combination of small and large particles can significantly improve green part quality. While the small particles fill the gaps between larger particles, the large particles enhance the spreadability of the powder due to their suitable flowability and together they can improve packing density which leads to increase in the number of contact points between particle, called as "coordination

number", and finally, results in the increase in the final sintered density [12,26,31,32,33,34]. Powder particle size also influences the minimum thickness of a layer, which is one of the key process parameters and it should be at least as large as the largest particle [5,12] to prevent large particles from getting pushed out of the powder bed.

The powder's morphology is another important factor by which the flowability, packing density, interaction between particles, the relative density of green part, and final sintered density are affected [22]. Most metal powders that have been used in AM are either water or gas atomized that each has different shapes of powders [5]. However, water-atomized powders (Figure 2.3b) with their irregular particles' shape are more common and economical in conventional P/M while gas-atomized powders (Figure 2.3a) with their spherical particles' shape have better flowability, spreadability [5,35] and sinterability [34] which makes them suitable but expensive option for powder bed AM technologies such as BJ. It has been reported that adding a low amount of lubricant (up to 2%), such as zinc stearate can enhance the flowability of powders with irregular particle shape. [36]

Some studies reported that by adding a small amount of some nanoparticles and suspend it into the liquid binder, the sinterability of printed parts can be improved as the ink-jetted nanoparticles can enhance densification as well as reducing sintering shrinkage and increasing mechanical strength. [37]

The tap density of powder has a direct effect on the bulk density of the powder bed. The lower tap density can lead to a higher amount of porosity, subsequently higher shrinkage rate and lower final sintered density [38].

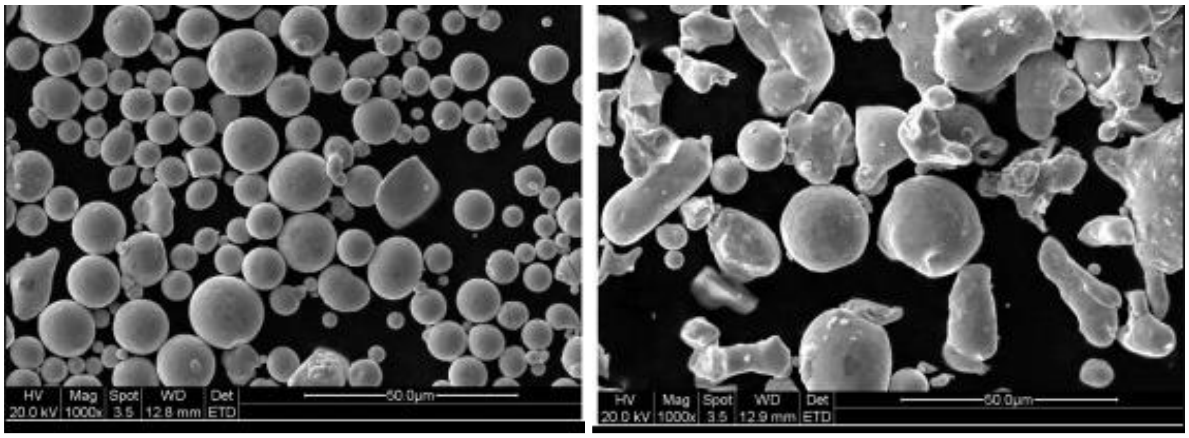

(a) (b)

Figure 2.3 SEM images showing characteristic morphologies of 316L SS powder; (a) gas atomized powder, (b) water atomized powder [35].

Binders

The binder that is used in the printing step is another critical pre-process parameter. In fact, it acts as a glue to stick powder particles into each other to shape the desired part and hold it until the initial stage of sintering. [39]. Similar to the powder, the binder directly influences green part quality as well as its density. [38]. Basically, the binder being used in BJ is organic-based which thermally decomposes and leaves a slight amount of residue. The amount of solid binder powder in the solvent, which can be water or alcohol, lies within the range of 1wt% to 10wt% [40]. With too much solid binder, the liquid binder cannot penetrate deep enough to adhere layers together. Without good layer adhesion, the green part will be too weak to handle It is vital for the binder to always maintain in the liquid phase as the dried liquid tends to cause blockage in the printhead [41]. In general, all amount of binder needs to be removed during the debinding step at the beginning of the heat-treatment process otherwise, any residual in the debinded part will turn into carbon at high temperature and hinder the diffusion during the sintering step leading to low final sintered density as well as weak mechanical properties[5,12,41].

Dislike scientific research studies, in the scope of the industry, changing the raw material features is neither an economy-wise nor a possible option, but recognizing these features can help to select the best raw materials. Taking into account this fact, it is better to focus more on

tailoring the process parameters in which the following section briefly mentions some of them in order to optimize and achieve a suitable green part.

2.1.2.2 Binder Jetting In-process Parameters

Knowing the fact that the BJ technology is more straightforward than other powder bed AM processes such as EBM and SLM, there are still some key parameters that should be recognized well in order to attain a suitable part regardless of what type of powder and alloy is used.
First and foremost, the part orientation in the printing step is a parameter that affects some final properties of the BJ manufactured part. Based on the literature, the part orientation noticeably influences the mechanical properties such as tensile and compression strength while a printed part is weaker in the perpendicular direction of the printing direction as the inter-layer strength is lower than intra-layer [11,42,43]. Thus, part orientation should be considered with respect to the application of the final part.

Another important in-process parameter is layer thickness. It has been reported that the layer thickness affects the amount of porosity inside the part [44]. In fact, by lowering the layer thickness the amount of porosity is decreased and the whole part sintered density is increased. [45] Moreover, it has been found that the layer thickness has an effect on tensile strength. [42]Also, the layer thickness has a significant influence on the shrinkage, distortion, and dimensional accuracy of BJ parts as the smaller layer thickness improves these parameters. [10] Additionally, using a medium-low layer thickness leads to obtain better surface roughness. [10] Similarly, by minimizing the layer thickness the higher density is achievable after sintering has done.[46] In general, reducing the layer thickness to an optimum size leads to an increase in green part density as well as obtaining a high quality printed part.[42]

Another important factor, which mainly affects compaction of powder bed and green part density is powder spreading speed and the rotating roller. [47]It has been shown that a higher spreading speed of the powder leads to a lower powder bed compaction, as well as bad surface roughness. It is also found that using a rotating roller overtakes a blade spreader in terms of the uniformity and compaction of the powder bed. [48] It has been demonstrated that Higher spread speed increases the amount of shrinkage and hence decreases the dimensional accuracy after sintering,

which is due to the low packing density and lack of uniformity of the spread powder. Also, lower spreading speeds and using rotating roller results in a higher strength in the green part.[48]

Drying time is one of the important factors during the printing step that should be taken into account to reach an ideal green part. As a matter of fact, the drying time in BJ refers to the period during which the jetted binder goes under the heater for drying after a layer is printed. Besides, during this time, the printhead goes to the cleaner tank for removing extra binders to avoid blockage happens. Therefore, insufficient drying time leads to printhead blockage in printhead as well as incomplete binder penetration into the powder layer, which subsequently deteriorates the part's surface quality and strength [10].

Furthermore, the amount of binder deposited into the powders, which is called binder saturation, to shape the green part impacts its density and dimensional accuracy. It has been reported that it is a critical parameter for predicting green part quality [49,50] Also, an optimized binder saturation leads to desired dimensional accuracy and green part density as the high amount of binder leaks out the designed layer and lowers both green part density and dimensional accuracy and low amount of binder results in lack of strength in green part. [10, 49,51] Besides, printing speed which is binder deposition speed affects dimensional accuracy. In fact, by increasing the binder deposition speed dimensional accuracy will be decreased and even some powder particles can get ejected out of the powder bed.[48, 52].

There are two general methods of pouring the binder onto the powder bed; drop-on-demand (DOD) and continuous-jet (CJ) [5,12,53]. In the DOD method, binder liquid droplets are shaped by applying electrical impulses through a piezoelectric or a thermal inkjet printhead [54,12]. Piezoelectric printheads work based on electrical stimulations that result in the deformation of piezo materials, which subsequently leads to generating pressure waves on the binder tank and form binder droplets [53,54] whereas thermal inkjet printheads vaporize the liquid and make the binder droplets to eject through volume expansion [12]. To avoid blockage of solid material in thermal printheads the vaporized liquid should dissolve again quickly [5]. On the other hand, in the CJ method, pressurized liquid binder jets out of printhead which makes this method more

useful for high-speed coverage of large surface areas while the DOD technology is more being used for spreading small and a more precise amount of binders [53].

All in all, there are some other factors such as drying temperature and time, roller leveling speed, printhead distance from the powder bed, etc. which contribute directly the green part quality and indirectly the final part properties. However, these parameters are machine design-dependent and fixed in a specific machine while varying in different machines. Thus, investigating these types of parameters is more beneficial for the machine design step, not process optimization. Preferably, studies on in-process parameters should aim at non-machine dependent process factors to reach beneficial conclusions for the general BJ process.

2.1.2.3 Binder Jetting Post-process Parameters

Debinding

In most BJ material systems, binders are based on organic compounds and burnt out during post-processing. The removal of the binder which is called *"debinding"* significantly affects the final part properties as the left residues hinder the densification during the sintering process. Basically, the debinding process usually is designed in a way that minimizes the amount of residues and adding an agent into the debinding process atmosphere such as oxygen or hydrogen, which can be reactive with the binder polymer, can accelerate the process [27,55] There are several types of debinding process in conventional PM processes including the direct thermal debinding and the catalytic debinding. In BJ, the thermal debinding process is used because of the type of binders, however, this process is slower than the catalytic one and needs enough time to let the evaporated/decomposed gas components inside the part escape to the atmosphere through pore channels. Defects such as blisters can be frequent unless suitable heating rates and enough times, such as several hours, are applied.[55] There are four key parameters by which the debinding process is affected; the heating rate, debinding temperature, hold time, and the atmosphere of the furnace. Those parameters depend on the type of binder material, which mostly affect the quality of a polymer removal, through evaporation or chemical decomposition. Basically, the hating rate and appropriate temperature(s) are selected based on the thermogravimetric analysis test (TGA) which represents the mass reduction of a test sample versus time/temperature. Also, the atmosphere is selected based on the removal mechanism and the powder alloy reactivity. For

example, oxidizing atmospheres can be detrimental for metallic materials while useful for binder decomposition. Thus, debinding in an inert atmosphere such as Argon or vacuum is more common. Although, reducing atmosphere such as Hydrogen, Nitrogen, and combination of each with Argon can be used based on the binder and powder alloy material in order to deoxidize or decarburize the green part from decomposed binder residuals. [55,56,57]

Generally, the debinding step associates with two main challenges. The first challenge is the heating rate and the time it needs to let the binder comes out from the core of a real industrial part since the high heating rate can result in crack formation due to the high pressure of decomposed/evaporated gas binder inside the green part. Second, the amount of residue that is left at the end of the debinding process, is crucial since it can be detrimental for the subsequent sintering process. Residuals from debinding can badly affect mechanical properties of the final part as well as hindering the diffusion between powder particles which results in a low densification rate and finally, a low final sintered density.[34, 55]
Although debinding information from PM somewhat helps the debinding process of BJ, more research needs to be done in order to tackle BJ's debinding challenges.

Sintering

Sintering is a thermal process used to bond contacting particles into a solid object. In industrial applications, sintering is a means to strengthen shaped particles to form desired objects such as metal cutting tools, electronic capacitors, automotive transmission gears, watch cases, and oil-less bearings. Having said that the sintering process is usually used as post-processing for parts made by conventional powder metallurgy as well as BJ-fabricated parts, the quality of the final parts once sintering is finished, usually depends on powder variables (size, additives, etc.), and the sintering condition such as the atmosphere of the furnace, temperature, holding time, heating, and cooling rate. [34,58]. Generally, the sintering process can be divided into four stages: Contact formation where weak atomic forces at particle contacts hold the particles together prior to sintering. This stage is usually ignored and not characterized as a separate stage during sintering by most publications. Neck growth is the first stage that each contact grows without dealing with neighboring contacts. Pore rounding is the intermediate stage where adjacent necks

enlarge and interact with each other to form a net of cylindrical pores. Pore closure is the last stage that cylindrical pores squeezed and closed to form separate spherical ones and then they shrink in order to reach high final densities. [34,59]

Similar to the debinding process, a sintering atmosphere should be selected based on the type of material and the properties that are desired while reducing or inert atmosphere are common to prevent oxidation, sintering can also be done in a vacuum to avoid trapped gas [34]. Generally, the main goal in sintering is to obtain a fully dense part close to 100% of theoretical density although, in some BJ applications such as biomedical implants fabrication, parts are intentionally made to have a porous structure [60,61,62]. Recently, it has been shown that high enough densities around 99% for BJ parts can be obtained after sintering.[3,63,64,] although it is more difficult in comparison with the conventional PM as the green density is usually lower in BJ manufactured parts. Consequently, it has been reported that reaching near full density (99%) after sintering, significantly improves the mechanical properties of BJ parts.[5] However, grain size coarsening is inherent in the sintering process, particularly in the last stage, at high temperatures.[34,88] Moreover, adding a small number of additive elements such as Cu nanoparticles can lead to a significant enhancement in BJ parts properties. [3,37,65] In fact, these nanoparticles act as agents which sit in powder particles interstices and lead to lowering sintering temperature. [37] Moreover, the shrinkage during sintering and mechanical strength are improved by using some transition metals in the powder bed such as Copper, Boron, Boron Nitride, and Boron Carbide which improve the final sintering density. [3] Finally, tailoring sintering parameters for BJ printed parts is based on the material and the desired part properties, which is comprehensively discussed in the following chapters of this work.

Infiltration as Post-sintering

One of the most common post-sintering solutions to reach near full density is infiltration. However, the compositional changes can be detrimental to the mechanical properties of the part. High and low-temperature infiltration mechanisms can be used based on the part material. The material used as an infiltrant should have a lower melting temperature than the main material to avoid the part from losing structural integrity during heating [12]. As an example, bronze which has a melting point of 950 °C is a suitable infiltrant material to fill the open pores of a sintered part that has a relative density lower than 92% and made from stainless steel with the melting

point of 1450 °C [3,5,11,34]. Also, infiltration can improve the mechanical strength of a sintered BJ part as it fills the interparticle gaps and eliminates the potential area for stress concentration. [66]

HIP as Post-sintering

Another post-sintering common option is Hot Isostatic Pressing (HIP) process. As a matter of fact, HIP can be used once sintering is done and reaching full density is needed. Unlike infiltration, HIP is used for the parts with isolated porosity that have more than 92% relative density and at temperatures lower than those that sintering happens. As mentioned, this process is useful for the parts without open porosities otherwise, since in the HIP process the pressure is uniformly applied on the part surface, nothing happens to the surface connected pores and hence, density will not increase. [68,5] Also, it has been reported that using HIP after sintering for BJ parts can enhance mechanical properties up to those of MIM fabricated parts, as well. [38].

2.2 Binder Jetting Material of Focus

Nowadays, BJ materials in-used range across some ceramics and metals. Generally, in comparison with other types of materials that have been used in AM processes, ceramic materials have low usage in AM products. In fact, a few types of ceramics such as Silica and Calcium sulfate are being used in the commercial AM. Having some properties such as high melting temperature, high thermal expansion coefficient, and low fracture toughness make them challenging material for the sintering-solidification process approaches such as BJ. Also, the binder jetting has been used to print green parts and based on the applications, they can be directly used such as sand molds and cores manufactured by binder jetting systems (e.g. ExOne, Voxeljet) for the sand casting industry. On the other hand, for the metal AM, particularly BJ, metallic powders are similar to the ones used in old-style powder metallurgy. However, besides some of the features that PM powder needs to have, there are some other specifications that suitable powders for AM powder bed processes such as BJ required to have such as powder spreadability. Plus, metallic powders are quite sensitive to moisture and easily oxidize although this does not mean that untouched powders in the powder cannot be reused for production. In fact, binder jetting supports the production of a much wider range of metal powders. Theoretically, BJ can handle almost all the powder materials which have a suitable binder

system. Although, because of the need for post-processing to reach desired mechanical properties, it is exposed to more constraints than other AM processes. All in all, the raw material options for AM are still somewhat limited due to some technical and non-technical reasons such as product cost and market demands. [68,69]

2.2.1 Stainless steel alloys

Stainless steel is a class of low carbon (up to 0.08 %) ferrous alloys which are known for its unique properties such as corrosion resistance, as well as its creep and oxidation, resist at high temperatures. In fact, as the chromium element in this alloy has a strong affinity for oxygen, the ability to form an ultra-thin film of chromium oxide on the surface makes the stainless steels resistant to corrosion. In practice, having a minimum amount of 10.5% Cr element in a ferrous alloy would define it as a type of stainless steel. However, there are a few types of stainless steel that have around 9% or more than 30% chromium element. Besides the chromium which is the key alloy element of stainless steel, there are also other essential alloying elements in each specific grade of stainless steel such as nickel, manganese, sulfur, molybdenum, titanium, silicon, carbon, and niobium. [70] As a matter of fact, these alloying elements are added to stainless steel for a special purpose such as strengthening, precipitation hardening, sensitization reduction, and improving their machinability. As time goes by, the demand for stainless steel increases since they have a variety of applications in aerospace, automotive industry, oil and chemical refinement, and biomedicine leading them became interesting alloys for the research domain. [71] Recognizing their properties as well as the proper processing techniques are critical to produce and select suitable stainless steel alloy powders for AM feedstock, particularly BJ.

Stainless steel grades

Stainless steel alloys are classified into four major families of ferritic, martensitic, austenitic, and duplex based on their main phase microstructure at room temperature, which is controlled by the amount of each alloying element. Ferritic stainless steels are alloys of iron and chromium which have a ferritic microstructure at room temperature. In comparison with other grades, ferritic stainless steels have less resistance to corrosion and lower strength at high temperatures. Although they have many applications as they are cheaper, have better magnetic behavior, better sinterability in PM parts, higher thermal conductivity, and a lower coefficient of thermal

expansion than the other grades. Martensitic grades of stainless steels are types of alloys that possess a martensitic crystal structure at room temperature. They exhibit high strength as well as fair wear and corrosion resistance therefore, they have been used once resistance to corrosion is required in combination with high strength at low temperatures or creep resistance at high temperatures. Austenitic grades are the most common types of stainless steels which offer superior resistance to corrosion compared to the other grades. These types of alloys also have applications in elevated temperature exposures. In general, austenitic stainless steels such as 316L still show acceptable corrosion resistance at high temperatures as 900 °C while ferritic and martensitic stainless steels lose their corrosion resistance noticeably at temperatures above 700 °C. Although austenitic stainless steels do not have suitable machinability, they exhibit a superior creep resistance. Duplex stainless steels or austenitic-ferritic stainless steel have two main phases of austenite and ferrite in their microstructure and carry some of the characteristics of both grades. Due to the amount of nitrogen and molybdenum, even some of the duplex stainless steels have better corrosion resistance than the austenitic grade such as 304L or 316L. Their excellent resistance to chloride stress-corrosion cracking, which is the Achille of austenitic alloys in the chemical and petrochemical industry, can be named as their superiority of these types of alloys. [70,71]

Application of 316L and its characteristics

In the 1960s the application of sintered stainless steel was widened up to industrial scale. Initially, sintered stainless steels served miscellaneous applications besides the fabrication of some automotive components. Among different alloys of stainless steel, 316L is one of the most commons that have had a wide application in the market. For instance, it has been used for the production of automotive parts, tools, electronics, and office equipment. [70] Also, 316L is one of the most common alloys in surgical implants from cardiovascular to orthodontic [71]. Besides, it is one of the most widely used materials in PM (powder metallurgy), MIM (metal injection molding), and nowadays in BJ for research and industrial applications because of the excellent mechanical properties of high corrosion resistance, high heat resistance, and good weldability. [73] From the microscale point of view, 316L stainless steel is austenitic steel with a little amount of ferrite due to having a high amount of nickel and a little bit manganese as an austenite

phase stabilizer at room temperature and low amount of carbon (around 0.03%) to increase ductility and minimizing sensitization and the formation of chromium carbide to reduce intergranular corrosion. [72,73] Figure 2.4 shows the micrograph of cast 316L which its phases can be seen there. [74] Table 2.2 shows the composition of 316L and based on the composition it can be mapped on Shaffler diagram Figure 2.5, to find out the phases it contains. Since 316L stainless steel is a highly alloyed material, the mechanical and corrosion properties are a concern therefore, obtaining a high final density that affects these properties is important for the optimization of the desirable attributes.

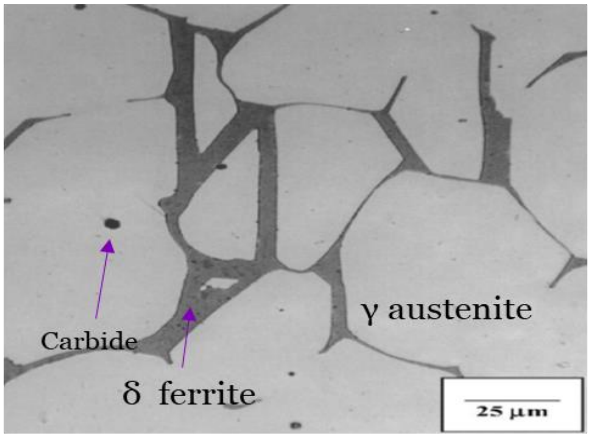

Figure 2.4 A micrograph of As-cast 316L showing austenitic matrix with a little amount of ferrite on grain boundaries and some carbides inside the grains [74]

Table 2.2 The composition of 316L stainless steel. [73]

C	Mn	Cr	Mo	Ni	Mn	P	S	Si	Fe
≤0.03	≤2.0	16-18	2-3	10-14	0.65	≤0.045	≤0.030	≤1.0	Bal.

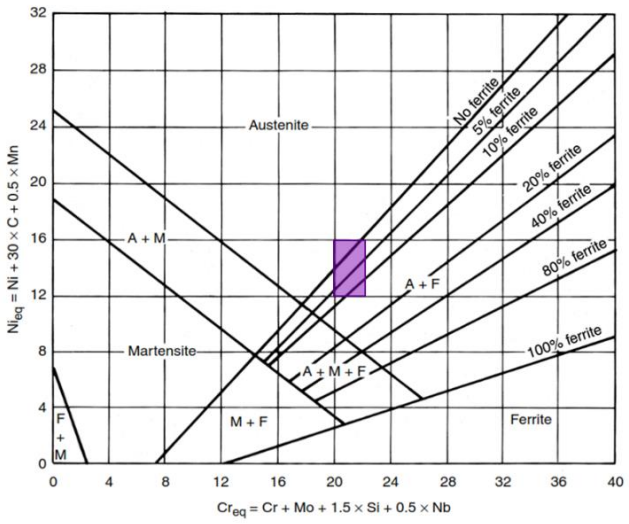

Figure 2.5 Shaffler diagram for alloyed steels, the purple-colored area is where 316L usually lay on, this diagram is based on the amount of Ni, Cr, and other elements.

2.2.2 Stainless steel powders

Generally, most powders that exist in the market are manufactured for conventional PM methods [76]. There are different methods for manufacturing powders while each of them results in specific properties for the powders and makes them suitable for a particular fabrication process. As an instance, the stainless steel powders made by water atomization have known as compacting grade and are capable of being cold-pressed in a die due to their irregular shape of particles[71] Moreover, gas atomized stainless steel powders have applications that need consolidation through hot pressing or extrusion [71]. Although the cooling rate in the water atomization process is way higher than the gas atomization, both have particles with homogenous microstructures and without segregation [71]. In fact, using suitable stainless steel powders as well as obtaining near full density lead to reaching unique parts that offer properties such as high fatigue resistance and impact strengths that are even better than properties attained by wrought stainless steel alloys [71]. Besides gas and water atomization, some other methods have been used for the fabrication of stainless steel powders such as centrifugal atomization which is useful for the fabrication of MIM grade powders. The most important features that should be taken into account for the production or selection of a stainless steel powder for BJ

process are nearly spherical shape and bimodal size which have a desirable flowability as well as suitable sinterability. [75]

So far, several different methods have been used based on their product features for the manufacturing of metallic powders but for BJ feedstock usage powder characteristics should be investigated in terms of the following conditions; (1) powder size range and its size distribution, (2) morphology of the powder (obtaining ideal sphericity), (3) powder particles surface, and (4) powder alloy chemical compositions. Table 2.3 presents these techniques as well as their specific features, advantages, and disadvantages.[77] However, because of some limitations in terms of process-material sensitivity, only a couple of them are applicable for stainless steel alloys; water, gas, and centrifugal atomization are the most commonly used processes in that regard. [78]

Table 2.3 Summary of powder characteristics based on the manufacturing process method. [77]

Manufacturing process	Particle size range (μm)	Pros	Cons
Water atomization	0-500	Low cost and high productivity	High amount of oxides, irregular particle shape, satellite exists, for non-reactive alloys
Gas atomization	0-500	Suitable for a wide range of alloys as well as reactive ones, spherical particles, high productivity	Satellite exists on particles, relatively high cost of production
Centrifugal atomization	0-600	Wide range of particle sizes with narrow PSD	Hard to achieve fine particles unless in very high speed
Plasma atomization	0-200	Ultra-fine and spherical particles	High cost and low productivity, wire or powder form of feedstock is needed
Plasma rotating electrode	0-100	High pure and spherical powders	High cost and low productivity

Centrifugal atomization method is a technique for the production of ferrous alloys powders such as stainless steel, through a rotating element. In practice, smooth, low oxidized content and low satellite, or even satellite-free powders can be obtained under a non-oxidizing atmosphere but need quite high rotating speed which reduces the productivity and raises the cost. Knowing the fact that centrifugal atomization is not a good option due to its disadvantages, remaining suitable options would be water and gas atomization. Although using the water atomized 316L powders are more economical than gas atomized ones, there are some drawbacks in this type of feedstock. In fact, water atomized powders have irregular non-spherical morphology which leads to bad rheological properties [79] as well as poor packing characteristics.[80,81] Besides, water atomized 316 L powder showed lower green density in comparison with gas atomized one with the same particle size.[80] Moreover, it has been reported that during the sintering of samples made from gas atomized and water atomized 316L with the same particle size, gas atomized powder samples reach higher density and exhibited lower shrinkage due to their spherical particle shape and higher green density. Also, because of the existing relatively high amount of oxides (especially SiO2) in water atomized 316L powders, H2O was produced and trapped as sintering proceeded and pores were closed, resulted in impeding full densification and pore annihilation. [80] All in all, from previous studies on BJ feedstock, it can be concluded that using a gas atomized powder which has a spherical particle shape with fine particle size and bimodal distribution would be the best option for BJ of 316L alloy. [5,75,82]

2.3 Sintering Theory

Human beings have been sintering ceramics and metals for thousands of years, but in practice, the comprehending of its fundamentals was started in the 1940s. The simplest example is when students in school work with wet clay to shape a pot, and then heat the wet pot to make it strong. That heating process is called sintering. In a similar way, freshly fallen snow bonds, will harden and eventually form ice, this is a cold version of sintering. In fact, until the last war, it was quite vague to people that what is going on in microscale and between particles to come up with a qualitative theory that involves the effective processing factors such as the temperature and time and relates them to an output parameter such as density or grain size. Sintering fundamentally characterized by the formation of sinter necks due to the reduction of the surface energy of

particles as the temperature rises. [34] In fact, the reduction of the surface energy happens due to removing the free surface and further with reducing grain boundary area via grain growth. This is the driving force in the sintering of most metals. It has been reported in many pieces of literature that the smaller particle size powder has more surface energy which leads to higher sintering rates and lower temperatures for neck initiation. Also, it is worth mentioning that in order to reach lower grain boundary energy, some grains rearrangement occurs. [34,83] The temperature needed to initiate the sintering mainly depends on the material, the green part compaction, and the particle sizes besides other parameters such as particle's morphology and surface's quality, heating rate, time, pressure, and atmosphere environment affect sintering behavior. [84]

2.3.1 Thermodynamics of Sintering

In 1945 the first theoretical model for the sintering of two spherical shape particles was offered by J. Frenkel [85]. In that model, the surface tension is assumed as a driving force that leads to mass transportation and filling the vacant space between two contacting particles and the mass flow considered be viscous Newtonian. This theory resulted in the creation of the relationship between the neck radius, X, formed between two contacting spheres with a radius of a, and the time of sintering, t:

$$\frac{X^2}{a} = \frac{3}{2}\frac{\gamma}{\eta}\,t \tag{2.1}$$

Where γ and η are surface tension and viscosity respectively. The false assumption behind this model was that the crystalline materials cannot exhibit Newtonian viscous flow. On the other hand, Frenkel's theory was implemented to powder compacts by Shaler & Wulff in 1948 [86] and introduced the plastic flow into sintering theory. They came up with an adjustable equation for densification during sintering. The general sintering equation that they offered for the formation of the neck between contacting spherical particles is:

$$\frac{X^n}{a^m} = F(T)t \tag{2.2}$$

Where n and m represent the mass transportation mechanism and F(T) is a function of temperature. If n = 2 and m = 1 Newtonian flow found by Frenkel's equation is dominant. For instance, if n = 3 and m = 1 diffusion is characterized by the evaporation from concavities and

condensation in cavities, volume diffusion is leading mechanism by n = 5 and m = 2, grain boundary diffusion by n = 6 and m = 2 and surface diffusion by n = 7 and m = 3. Further, in 1949, Kuczynski [87] offered a sintering model for two contacting spherical particles, which turned out to be the most acceptable theory. [34, 88]. In that model, he claimed that the mass transport mechanism in the sintering of metals is due to the lattice (or volume) diffusion and mostly the volume diffusion is dominant. Nonetheless, in 1967, Rockland [89] suggested for the sintering of metallic materials that the grain boundary diffusion is the dominant mechanism while atoms diffuse into the interstitials through grain boundaries.

It is worth mentioning that diffusion is playing the main role in the sintering process and it is a temperature-dependent process [34]:

$$D = D_0 \exp(-\frac{Q}{RT}) \tag{2.3}$$

where *D* and *Do* are diffusion coefficient and diffusion constant, respectively with the same unit of (cm^2/s), *R* is the universal gas constant (8.314 J/mol·K), *Q* is the activation energy (J/mol) for diffusion, and *T* is the temperature (K).

2.3.2 Kinematics of Sintering

During the sintering process, contacting particles bond to each other by some diffusion mechanisms at a temperature below the melting point, which is also known as solidus sintering [34]. Similarly, sintering can be conducted in higher temperatures than the solidus phase, which are known as liquidus and super-solidus phase sintering. In the solid-state sintering, diffusional mechanisms control the process and because of that, it needs relatively high time. In super-solidus and liquid phase sintering, due to the presence of liquid, the sintering process is carried out faster with a higher densification rate [34]. More specifically, most of the sintering processes in the industry of metal powder metallurgy applications are conducted in the liquid phase, particularly for multi-material systems and alloys as it offers better control on microstructure. Nevertheless, microstructural softening takes place in the liquid phase sintering and causes distortion and loss of shape fidelity. [91] Thus, this type of sintering regime was not chosen for the sintering of BJ samples in this piece of work. Supersolidous phase sintering theory first proposed by German [92] in 1990. In fact, by elevating the temperature to above solidus and

below liquidus points, a liquid fraction is created within the powder compaction which subsequently wets the solid phase and enlarges the sinter necks. As phase diagrams could be up to 50 C off, it is recommended to use DSC curves to find out about the sintering temperature. [34] However, a quite accurate measurement of the temperature needs to be done to prevent the melting of the whole compact which is a vital point that should be taken into account for the sintering of BJ samples. Since it is hard to control the amount of liquid phase, this type of sintering regime is not used for this research and thus the solid-state sintering was selected in this piece of work.

2.3.3 Solid-state sintering

As mentioned before, solid-state sintering occurs at the temperatures below the solidus point where the material is in the solid phase. The solid-state sintering includes different stages and is conducted through mechanisms that are mainly based on atomic diffusion. However, not all the diffusion mechanisms result in densification and shrinkage. The densifying mechanisms are the ones that lead to bulk transport of atoms such as grain boundary diffusion, lattice (volume) diffusion from grain boundary, and plastic (viscous) flow. On the other hand, some diffusion mechanisms including surface diffusion, evaporation-condensation mechanism, and lattice (volume) diffusion from the particle surface to the neck area cause neck growth without any densification. Figure 2.6 schematically shows the bulk and surface transport mechanisms of atoms during sintering. The dominance of non-densifying mechanisms in sintering leads to obtain a porous microstructure [34,92].

Densifying:

- Plastic flow (dislocation climb or glide)
- Grain boundary diffusion
- Lattice (volume) diffusion (from grain boundary)

Non-Densifying:

- Evaporation-Condensation
- Surface diffusion
- Lattice (volume) diffusion (from grain surface)

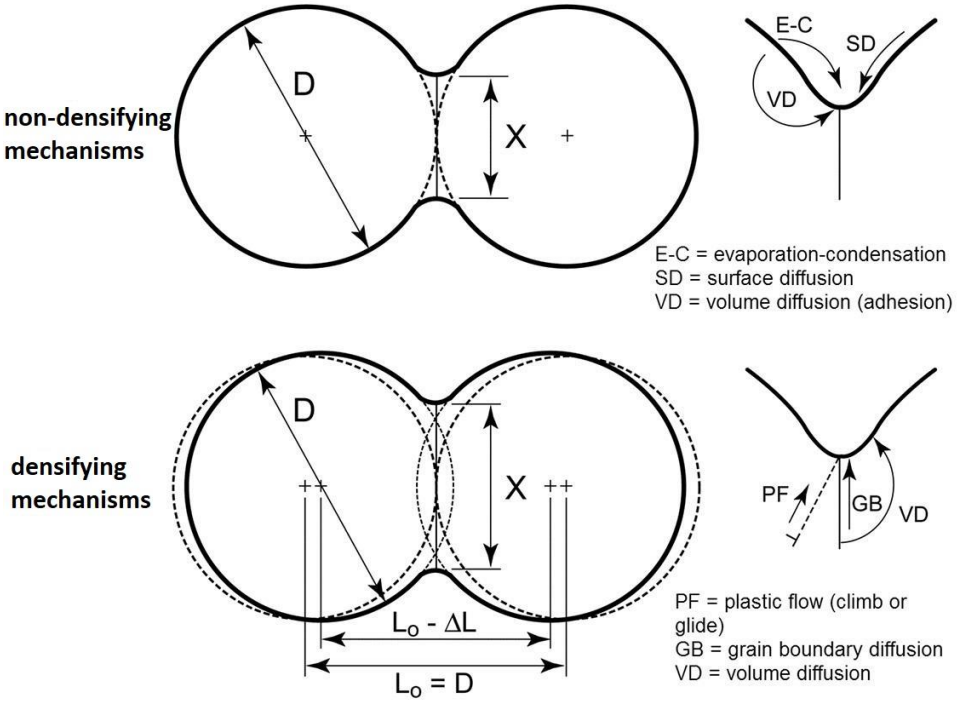

Figure 2.6 Diffusion mechanisms in sintering models for two contacting spheres with diameter D. The first sketch displays neck growth measured by the neck diameter, X, through surface transport mechanisms that do not lead to densification. The second sketch shows diffusion through bulk transport mechanisms that lead to mass-transportation, associating with shrinkage, between contacting particles to create densification. [34]

2.3.4 Stages of Sintering

The stages during sintering show the geometrical progress of transforming a weak powder compact into a solid body. Based on the conditions that sintering is started; the sintering stages might begin with loose or deformed powder particles. The first one is the case for parts formed using slip casting, injection molding, extrusion, tape casting, and BJ. Particle deformation to give a high starting density is associated with high-pressure forming, such as die compaction, cold isostatic pressing, and cycles that pressure is applied prior to sintering. In sintering models, particles are assumed to be spherical, start with point contacts between particles close to each other. [93]

Based on phenomenological observations, sintering is divided into three overlapping stages:

• Neck growth; the first stage that each contact between neighbor particle forms and grows without an eye-catching change in volume. Surface diffusion is more dominant in this stage.

• Pore rounding; the intermediate stage in which adjacent necks enlarge and interact with each other to form a net of cylindrical pores. In this stage, the pores become interconnected and the accompanying reduction in curvature and surface area causes a slower rate of sintering. Grain boundary diffusion is the most principal mechanism here.

• Pore closure; the last stage that cylindrical pores squeezed and closed to form separate spherical ones. In the final stage, the densification rate is slow and the grain growth is obvious. Plastic flow and volume diffusion are the most prominent in this stage.

Figure 2.7 shows these sintering stages. The first stage starts with interacting particles while a neck growing by short atomic motion. Simultaneously, a grain boundary shapes at the neck area, as the grains have random crystal orientations with respect to each other. Those necks are saddle surfaces owing to the combination of concave and convex surface curvatures existing. Figure 2.8 shows a scanning electron micrograph(SEM) of the neck growth during sintering.

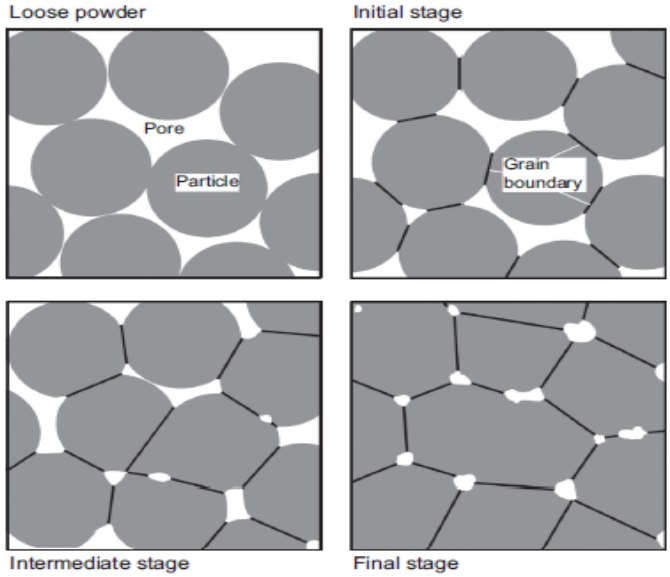

Figure 2.7 Graphical representation of the sintering stages [34]

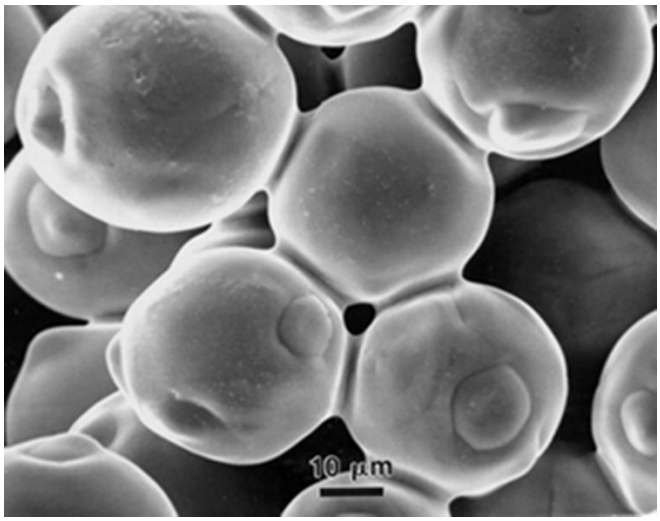

Figure 2.8 Scanning electron micrograph of neck growth for sintered spherical 32 μm nickel particles [34]

Figure 2.9 clarifies how the necks grow during sintering as time goes by. From empirical observations, adequate holding time in sintering at a proper temperature is needed to let particles diffused to each other. [34]

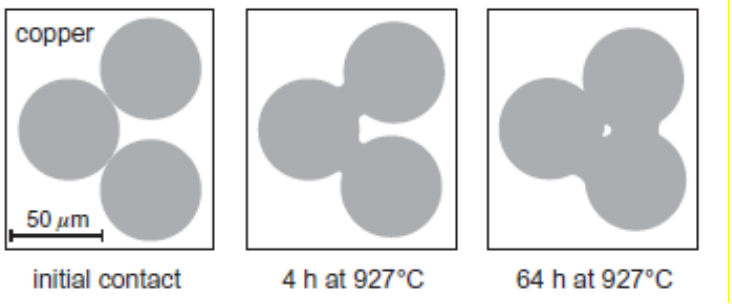

Figure 2.9 Neck growth during the sintering of copper particles [34]

All in all, knowing the fact that the relative green density in BJ products is around 60%, during the sintering, the initial stage results in up to 2% shrinkage due to the neck formation between particles. Nevertheless, at the end of the final stage of sintering, up to 20%, linear shrinkage can be seen. Adding a short amount of sintering additives can improve the sintering process by enhancing particle bonding before the initial stage of sintering. Plus, sintering additives affect grain growth during the sintering process. In more detail, they enhance surface diffusion rate, as

well as improving lattice and grain boundary diffusion while they resist grain boundary mobility and weakens grain surface energy during the sintering process [34,37,94] Also, using a mixed distribution of large and small particles can profoundly promote densification behavior during the sintering of BJ products [5,12,28].

2.4 Analytical Model

Sintering of powder particles is a thermal process that involves the mass-transport phenomena resulting in the particles get bounded [95]. The mass-transport phenomena which lead to densification in the compact of particles are due to reduce the free surface energy between them. The surface diffusion mechanisms only form the initial bonding between particles which is called "necks" during sintering. Following the surface diffusion, grain boundary and volume diffusion mechanisms progress and increase the density of BJ printed part by diffusing its powder particle into each other to reduce the free surface energy.

2.4.1 Combined stage Sintering Theory

Hansen et al. [96] developed a combined-stage sintering model for solid-state sintering by studying the mass-transport mechanisms during sintering, which let them predict both the shrinkage and densification during sintering. In their work, the grain boundary and volume diffusion were assumed to be the reason for densification resulting in the combined-stage sintering equation:

$$-\frac{dL}{Ldt} = \frac{\gamma\Omega}{kT}\left[\frac{\Gamma_v D_v}{G^3} + \frac{\Gamma_b D_b}{G^4}\right]. \tag{2.4}$$

In the above equation L is a representative dimension, t is time, Ω is the atomic volume, γ is the surface energy, T is the temperature, k is Boltzmann's constant, Γ is a lumped scaling factor, D is the diffusivity factor, G is the grain size, and the subscripts ν and b are volume diffusion and grain boundary diffusion factors, respectively. On the other hand, the lumped scaling factors, Γ_v and Γ_b are the density-dependent geometric terms as well as D, the diffusivity factors which should be determined from experiments for a specific sintering system. Assuming that the

shrinkage is anisotropic while the mass does not change in sintering, the following equation can be obtained:

$$-\frac{dL}{Ldt} = \frac{d\rho}{3\rho dt}. \tag{2.5}$$

By combining (2) and (3) Su and Johnson [97] rearranged the *combined-stage sintering equation* through piling all the density-dependent material parameters on one side, while the known process-dependent parameters except the Q which is apparent activation energy on the right side:

$$\frac{k}{\gamma \Omega_a D_0}\int_{\rho_0}^{\rho}\frac{(G(\rho))^n}{3\rho\Gamma(\rho)}d\rho = \int_0^t \frac{1}{T}\exp\left(-\frac{Q}{RT}\right)dt. \tag{2.6}$$

Here, D_0 is the apparent diffusivity factor representing the diverse influence of both the volume and grain boundary diffusion mechanisms. The left side is considered as the increase of internal energy because of the increase in the density of the system during the sintering process. Similarly, the right side of the above equation is considered as the energy that deposited to the system during the process. Now, the right side can be introduced as a term(Θ), work of sintering, as follows:

$$\Theta(\mathrm{t},\mathrm{T}) = \int_0^t \frac{1}{T}\exp\left(-\frac{Q}{RT}\right)dt. \tag{2.7}$$

In the above equation, the value for apparent activation energy is necessary to evaluate the work of sintering (Θ) can be determined through numerical analysis. Guessing an initial value from previous works and giving it a wide range, it can be found through iteration. In this study, the proper value for Q was found through iteration using the least-squares norm of residuals method, equation 2.8, which is a statistical approach to find the best value that fits well the experimental data into the combined stage sintering model.

$$\min(\chi^2) = \sum_{i=1}^{n}\left(\frac{\rho_{measured,i}-\rho_{calc,i}}{\rho_{measured,i}}\right)^2. \tag{2.8}$$

where $\rho_{measured}$ refers to the experimentally measured relative density, and ρ_{calc} refers to the predicted value from the combined stage sintering model. Based on the model, it is clear that at a

given time t there should be an apparent density of ρ corresponding to a work of sintering of Θ. [97]

2.4.2 Master Sintering Curve

As mentioned before, the sintering process is influenced by many material-based and process parameters, which make it difficult to predict the sintering behavior. Therefore, an empirical tool to present the sintering behavior without accurately measuring material parameters was needed for the powder metallurgy community. This concept is called the Master Sintering Curve (MSC) which presents the relationship between the relative density during the sintering and the work of sintering based on the equation 2.7. In more detail, the MSC is capable to predict the final density of sintered products as well as the comparison between the densification behavior of different powders during the sintering process. Based on previous studies, a sigmoidal function is the best choice that describes the relationship between the apparent density and work of sintering. [90,98,99] Consistent with this, the apparent relative density ρ measured from the experiments has a sigmoidal relation with the work of sintering as follows:

$$\rho = a + \frac{(1-a)}{1+\exp(-\frac{(ln\Theta-b)}{c})} . \quad (2.9)$$

In the above equation *a*, *b*, and *c* are constants that define the sintering curve for the system. Constant *a* is the relative density of the green part. Constants *b* and *c* depend on the material.

An Example of MSC for Inconel 718 alloy and the plot of residuals for different values of its apparent activation energy is shown in Figure 2.10. It was found that the apparent activation energy Q is affected by heating rate[100], powder particle size[33], and any other parameter that has an effect on sintering behavior. In fact, most pieces of literature that discuss the MSC are rather related to conventional PM processes than BJ. Implementing the MSC to establish an empirical comparison for the sintering of BJ samples is part of this thesis.

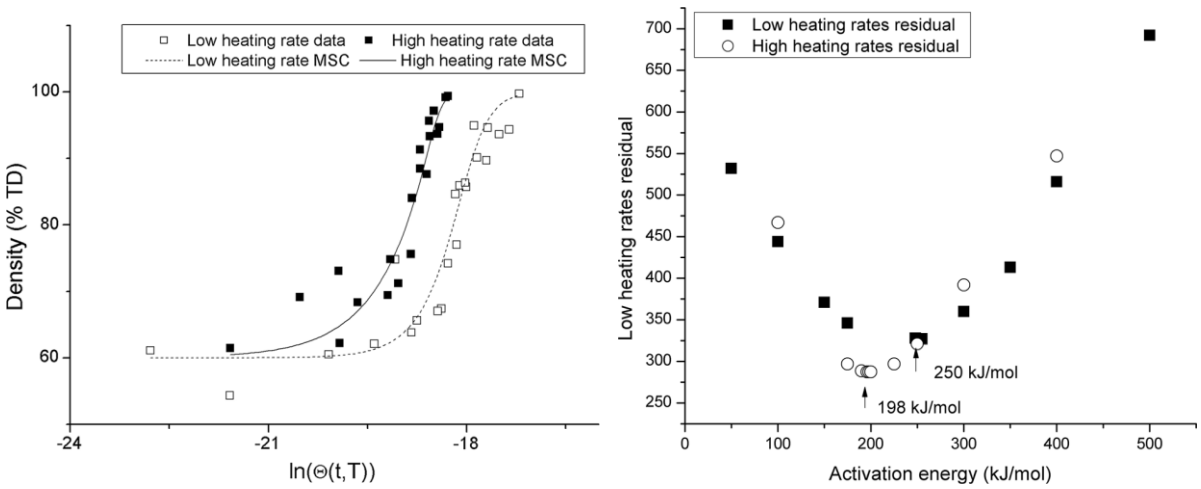

(a) (b)

Figure 2.10 (a) Master sintering curve for Inconel 718 alloy and (b) the plot of residuals [100]

Chapter 3

Materials and Methodology

The methodology of this thesis relies on three different powders and a binder as raw materials, besides set of characterization tests as well as some density measurements on both raw materials and final processed samples. The powders are made of 316L stainless steel alloy with three different particle size distribution. The binder for this study was a patented liquid binder that was provided by the General Electric Company, additive manufacturing division (West Chester, OH).[109] For the characterizations, scanning electron microscopy (SEM) and a set of powder characterization tests were done. Moreover, thermal gravimetric analysis (TGA) as well as the differential scanning calorimetry (DSC) were used to design an optimum heat treatment profile. Further, Archimedes density measurement was applied to measure the final density of samples after sintering. Finally, the measured density data were collected and undergone a statistical refinement practice to be prepared for MSC which is an empirical tool to examine the sinterability of each powder.

3.1 Materials

3.1.1 316L Stainless Steel Powders

In this study, three different 316L stainless steel powder were used. Those powders vary in terms of their particle size. All the powders were gas-atomized which means that a typically spherical morphology had to be expected for their particles. Table 3.1 shows the info for the powders as well as the nominal particle size distribution from the supplier company. The three powders are referred to as unimodal fine (UMF), bimodal coarse (BMC), and bimodal fine (BMF). Each powder had blended by a rotary blender (Thumler's A-R12) for 15 min to have a fine distribution before usage.

Table 3.1 The 316L powder types and their nominal particle sizes

Powder designation	Nominal particle sizes (µm)
UMF	0-22
BMC	5-45
BMF	5-45

3.2 Powder characterization

Similar to any other manufacturing process, characterization of raw materials which in this work are metallic powders has been always a need to assess the impact of the powder characteristics on the process and the final part. Generally, the important powder characteristics that should be inspected in AM are flowability, particle size distribution, morphology, and tap density. [55,77,78]

3.2.1 Particle Size Distribution (PSD)

For the powders that were used in this thesis, the particle size distribution analysis test was done using the CAMSIZER X2 system (RETSCH, Wuppertal, Germany) which works based on the digital image processing of pictures, 300 per second, taken from powder particles. As it can be seen in figure 3.1, The CAMSIZER X2 uses a simple patent; dispersing powder particles in front of two bright LED light sources and The shadows of those particles are taken by two high-speed cameras. While the basic camera is for the detection of the big particles with a large field of view, the zoom camera is installed to scan smaller particles with high resolution. Further, a user-friendly software analyzes the size and shape of the particles caught by the cameras and finally giving away the distribution of each class size particles. For the work of this thesis, a set of hundred particle class size from 0.1 µm to 100 µm was defined to classify each powder particle size distribution.

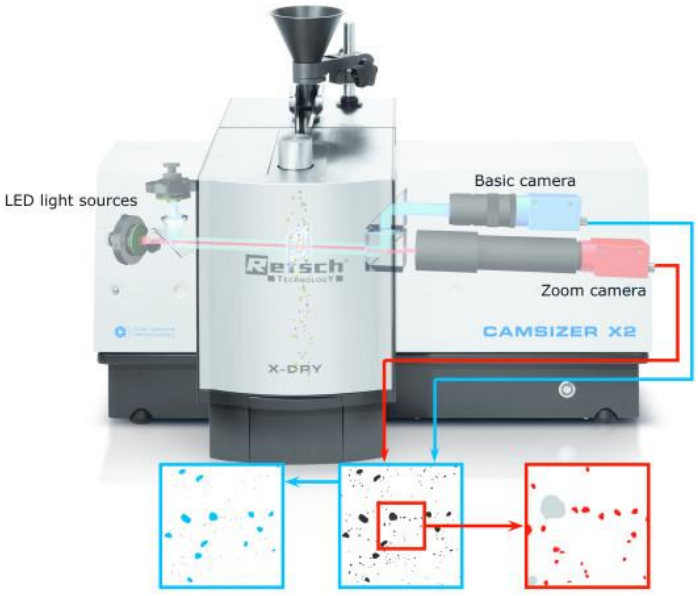

Figure 3.1 The CAMSIZER X2 system from RETSCH and the way that it captures the powder particles [101]

3.2.2 Stability & Flowability

As a powder bed AM technology, BJ requires a powder material with perfect spreadability. Powders with weak flowability, cannot be spread smoothly and uniformly onto the bed and lead to defects in the part structure during the printing step. In order to find out the rheology of the powders, the rheometry test was done using the FT4 powder Rheometer system (Freeman Technology, Welland, UK), figure 3.2. From the test analysis and interpreting some factors, the flowability of powders was examined. In more detail, the FT4 employs the technique of measuring the powder resistance to flow. During the test, a ‘blade’ starts to rotate and moving downwards through the powder to establish a flow pattern with 11 different flow patterns for each trial. This leads to thousands of particles to interact, slide, or flow over another, and the amount of resistance energy that the blade face from the powder, shows how they are hard to flow. For the powders used in this thesis, two sets of trials were done and the average was taken as the output data.

Figure 3.2 The FT4 powder rheometer system and the flow pattern that its blade create [102]

3.3 Powder sintering experiments

3.3.1 Sample Fabrication

Green samples from three different powders were fabricated using cubical silicone molds with the approximate dimensions of 1 $cm \times 1\ cm \times 1cm$. The powder is added to the silicone mold layer by layer. For each layer, the liquid binder was dropped with a pipette until it reaches the powder surface. To accelerate the spreading of binder, removing the trapped air bubbles and flattening the sample surface, the silicone mold was placed on a benchtop vibrator for a minute. This process is iterated until the powder fills the silicone mold. Then, the silicone mold is left on a hot-plate overnight at 100 °C to remove the binder solvent. The dried green sample is removed from the silicone mold gently and inspected to see its integrity. Figure 3.3 illustrates the sample fabrication procedure and a green sample.

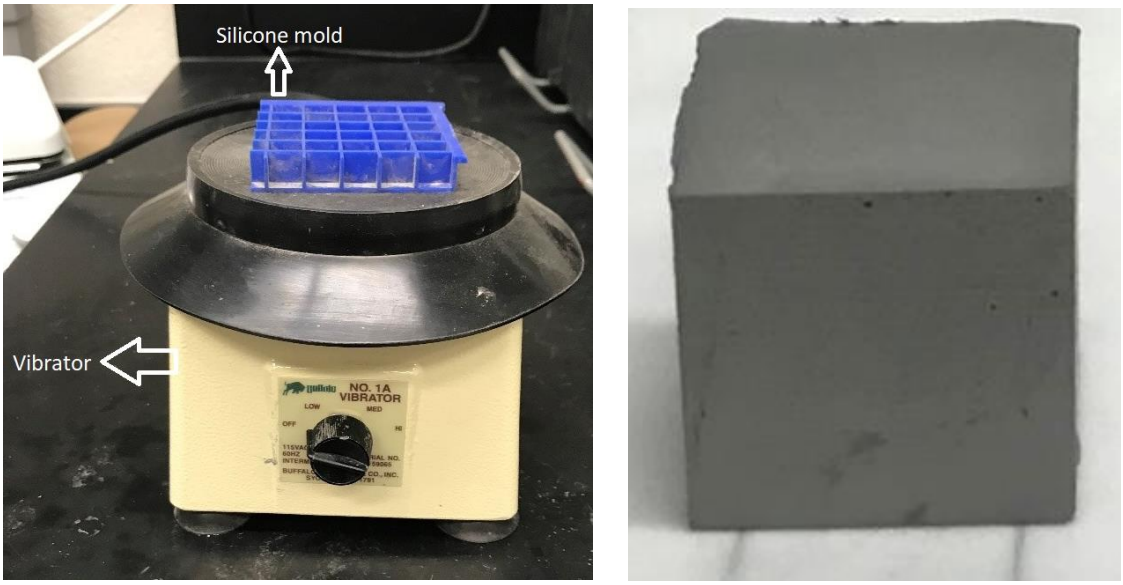

a) b)

Figure 3.3 Sample fabrication facilities; a) silicone mold and the vibrator. b) a dried green sample with ~1cm^3 dimension.

3.3.2 Heat Treatment

As discussed in the late chapter, the properties of the final part highly rely on post-processing parameters. The post-processing procedure in this thesis includes debinding and sintering. Once sample fabrication finished, the dried green samples were undergone to a thermal heat treatment in the GSL-1600X-50-UL tube furnace (MTI Corporation, Richmond, CA) which is shown in figure 3.4, with a specific heat treatment profile. The heat treatment profile was designed based on the thermal behavior of both binder and powder materials. In the following sections the debinding and sintering analysis which resulted in an optimum heat treatment profile, are discussed.

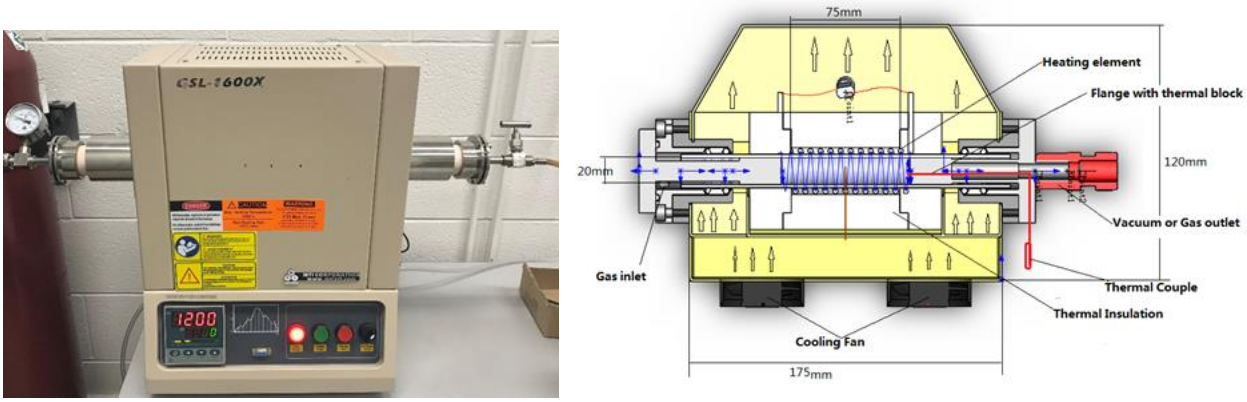

(a) (b)

Figure 3.4 (a) the MTI GSL-1600X-50-UL Tube furnace and (b) the illustration of its different elements [103]

3.3.2.1 Debinding

As the first step of post-processing, debinding plays a vital role in the BJ process. Knowing the fact that inadequate debinding can lead to detrimental defects in the final part, the debinding should be designed in a way that results in the minimum amount of residue. Based on the type of material, fully thermal debinding is used for the BJ debinding. In that regard, the mass reduction based on the temperature was studied for the binder in order to find the initiation temperatures for the debinding step.

3.3.2.1.1 Thermal Gravimetric Analysis (TGA)

Thermal gravimetric analysis (TGA) test method was used for the study of the debinding step. For that purpose, a small amount of cured binder was prepared with the net mass of 24.4 mg in an alumina crucible. Further, the sample was placed into the STA 449F1 TGA system (Netzsch, Burlington, MA), which is shown in figure 3.6, under a 95% Ar-5% H2 atmosphere. Due to the limitation of the changing atmosphere during the heat treatment process, the atmosphere of debinding was selected to be similar to the sintering step. Using the TGA test system, the sample was heated from room temperature (24 °C) to 800 °C, where approximately is the point before the sintering sarts [33], with a constant heating rate of 10 °C/min. Leaving less than 10% of the binder by the end of the experiment, the debinding initiation temperatures as well as the duration

were obtained from the TGA curve to guarantee a reasonable optimum debinding step in the heat treatment profile.

3.3.2.2 Sintering

Based on the material and geometry accuracy, the solid-state sintering regime was chosen for the samples in this research. It was vital not to pass solid-state during sintering since the shape fidelity would get lost. In that regard, the solidus temperature in the phase diagram of the 316L alloy was required in order to know the maximum temperature that was the limit in the heat treatment profile. Figure 3.5 shows the phase diagram for the alloy where the solidus point is around 1400 °C. [104] Although the phase diagram provided a reasonable estimation for the sintering temperature limit, the difference in their PSD can lead to a difference in their solidus point. [105] Therefore, the thermal behavior of each powder had to be studied.

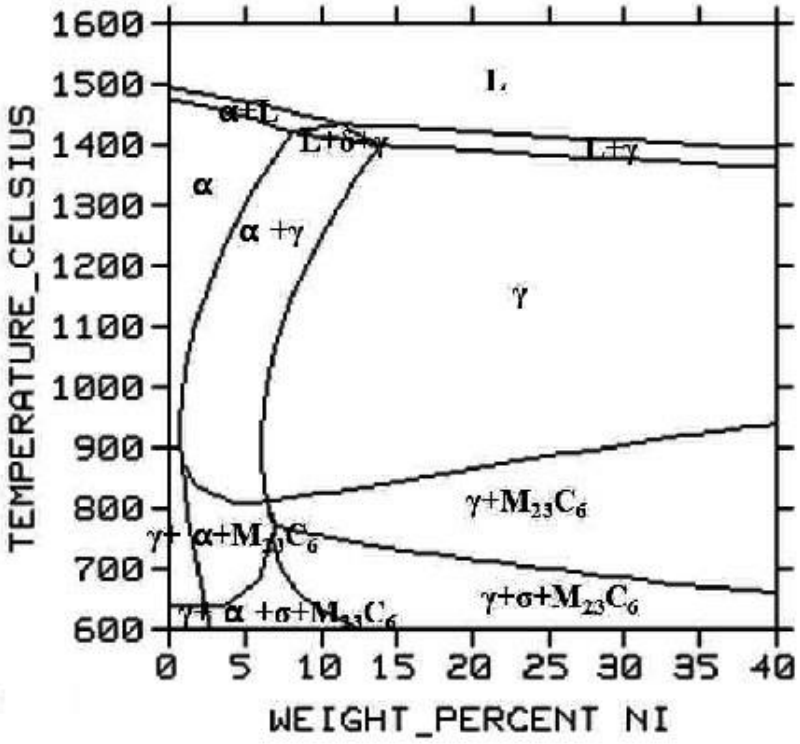

Figure 3.5 The phase diagram of commercial 316L stainless steel [104]

3.3.2.2.1 Differential Scanning Calorimetry (DSC)

Differential scanning calorimetry (DSC) experiment was done to precisely capture phase transformation versus rising temperature in each powder. For that purpose, the amount of 158 mg of powder was put into an alumina crucible with 350 mg mass. Besides, another empty crucible was used as the reference sample since the DSC works based on the difference in energy consumption of the test sample with a reference sample that does not have any phase transformation in the temperature range that the experiment is done. Further, both the reference and test samples were put into the same system that the TGA test was done, the STA 449F1 DSC system (Netzsch, Burlington, MA), which is shown in figure 3.6, under a 95% Ar-5% H2 atmosphere with the constant heating rate of 10 °C/min. Similar to the TGA, the gas atmosphere was selected regarding the availability and safety restrictions for use in the very heat-treatment process. From the DSC diagrams, solidus points in both heating and cooling were obtained and they were considered for the heat treatment profile of the fabricated green samples.

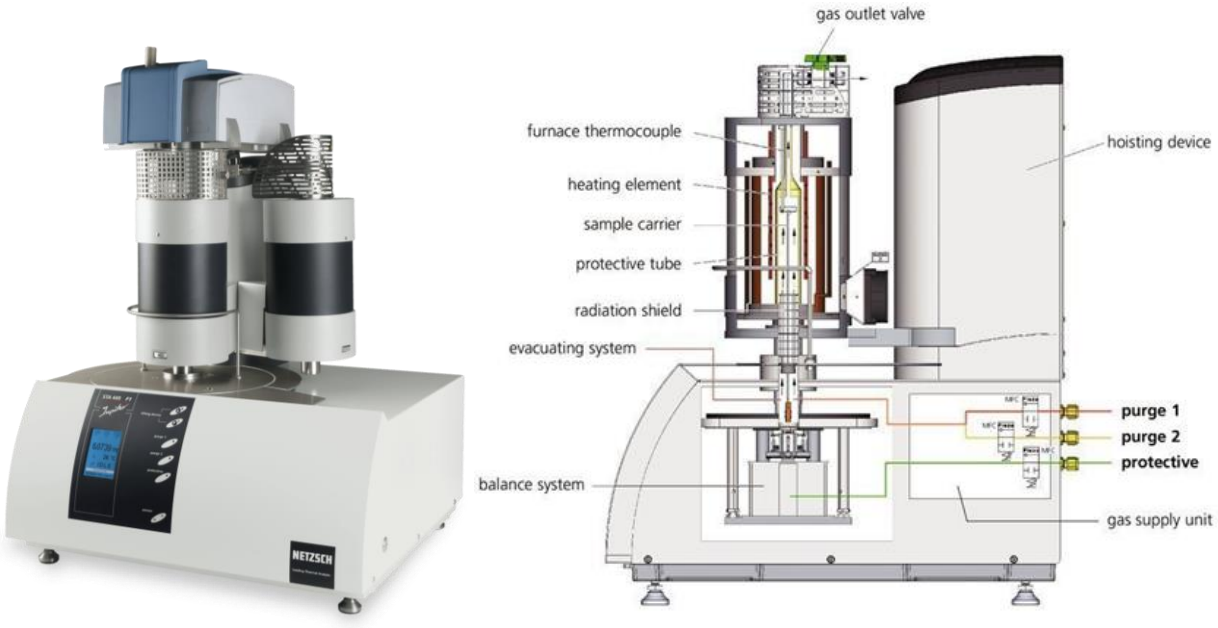

Figure 3.6 The STA 449F1 DSC/TGA system from NETZSCH [106]

3.3.3 Heat Treatment Profile

As mentioned before, the heat treatment process was performed using a tube furnace (MTI GSL-1600X-50-UL) while the framework was defined based on the results from TGA and DSC (Netzsch Jupiter STA 449 F1) experiments. From these experiments and previous works, temperature, time, and the gas atmosphere inside the furnace were selected for the heat treatment process based on the materials. The processes generally consist of three stages: drying, where the green samples were placed into an oven to let the solvent get evaporated from the samples at relatively low temperatures (up to 100 ℃). Debinding, where the binder removed at moderate temperatures (up to 500 ℃). In the end, sintering was conducted at high temperatures (up to 1400 ℃) where shrinkage and densification take place. The multi-stage profile has been defined where the temperature was shortly held for intervals in order to dedicate enough time for thermodynamic and mass transportation phenomena to get accomplished. This is the general experimental approach that was taken in this study. With respect to the safety restrictions, both debinding and sintering were executed in 95%Ar–5%H_2 atmosphere while the hydrogen acts as a reducing agent, it breaks the oxide layers that exist on powder particles' surface,[55] thereby improving the formation of sinter necks between particles [5]. The process started from room temperature with a heating rate of 10 ℃/min up to 310 ℃. The samples were kept at this temperature for 30 min, then were heated to 430 ℃ with the same heating rate and stayed there again for 30 min to enable decomposition of the binder. To carry out sintering, first, the samples were heated up to 900 ℃ with the ramp of 10 ℃/min. Subsequently from this temperature they ramped up at 5 ℃/min to a variety of higher temperatures with different holding time (0-10 hours) then cooled down to room temperature. Figure 3.7 schematically shows the heat-treatment process used in this study. The details about the debinding and sintering temperatures with different holding times are presented in Table 3.2.

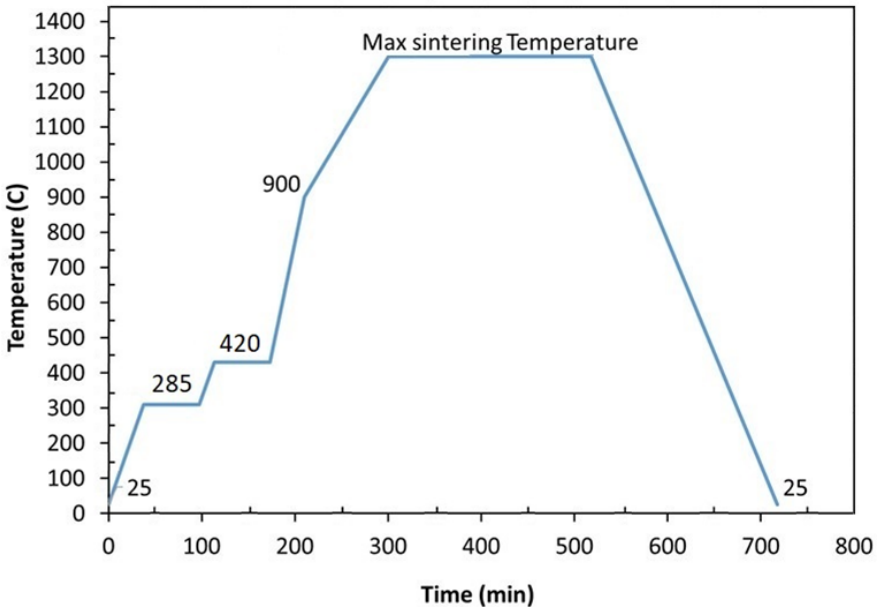

Figure 3.7 The heat-treatment profile for the test samples

Table 3.2 the heat-treatment procedure features

Sintering temperature range(°C)	Holding time range(min)	Debinding temperature range(°C)	Heating rate(°C/min)
900-1400	0-600	310-470	5-10

3.4 Density Measurements

3.4.1 Powders Density Measurement

Since the powders have different PSD, during the atomization process they might catch different amount of gas trapped inside their particles that affects their density. Besides, in powder metallurgy, green and sintered densities usually are shown as the term "*Relative Density*" which is the ratio of measured density to the real density of the alloy. In order to determine the real density of the powders the gas pycnometry test was done using the ULTRAPYC 1200E gas pycnometer system (Quantachrome, Boynton Beach, FL) shown in figure 3.8. The pycnometer system works based on measuring the true volume of the solid powder by implementing the Archimedes principle for fluid displacement and Boyle's Law for gas expansion. In this measurement system, a gas is used as the fluid since it can easily penetrate the smallest pores to

obtain high accuracy. Thus, Helium was used as the displacing gas because of its small atomic dimension which leat it to penetrate to pores with a 0.2 nm dimension while as an Ideal gas it does not react with any material during the test. [107]

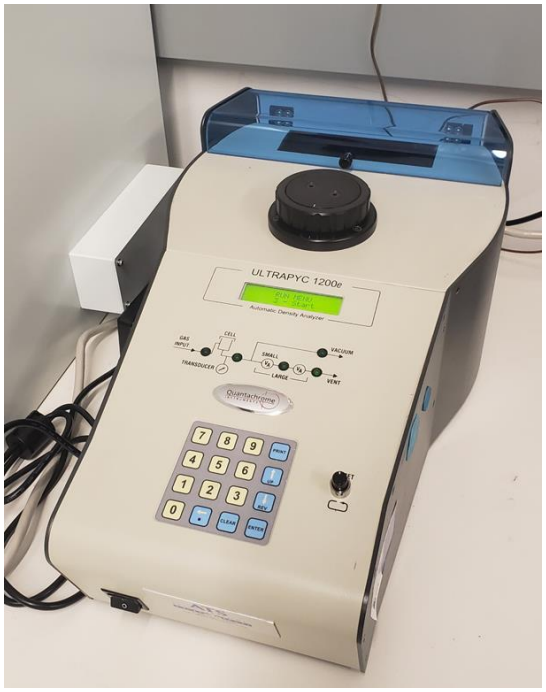

Figure 3.8 The ULTRAPYC 1200E gas pycnometer system from Quantachrome that used for powders density measurement

3.4.2 Green Samples Density Measurement

The initial assessment for the density of fabricated samples was determined through mass and geometry measurements. The mass measurements were done using the analytical balance (Adam Equipment Inc, Fox Hollow Road, Oxford, CT) with $\pm\, 0.0001\ g$ and geometrical measurements were performed by calipers (Mitutoyo Absolute Digimatic Caliper, Mississauga, ON). Further, the green density is estimated by using Equation 3.1, where *m* is the mass of the sample, and *a*, *b*, and *c* are the diameters of each cubical samples. The average value of three different points measurement was taken for each side to reduce errors in the measurement.

$$\rho_{green\ sample} = \frac{m}{a*b*c}\ \left(\frac{gr}{cm^3}\right). \tag{3.1}$$

3.4.3 Sintered Samples Density Measurement

The bulk density of each sintered sample was quantified using the average of three measurement repetitions. For that purpose, the Archimedes method was chosen and measurements were performed based on ASTM B962 – 17 [108] which is the standard for measuring the density of PM and sintered samples. Knowing the fact that sintered samples usually have some pores which are open to the surface, the small amount of the high vacuum grease (Dow Corning, Mississauga, ON) was added on the surfaces in order to prevent the liquid to penetrate in and obtain a reasonable accuracy. Samples' weights were measured, once in the air and once it was immersed in water by the analytical balance and Archimede test kit (Adam Equipment Inc, Fox Hollow Road, Oxford, CT) shown in figure 3.9 with $\pm\, 0.0001\ g$ accuracy. Further, by implementing the equation 3.2, the bulk densities of the samples were determined while the temperature was monitored to reach precise results.

$$\rho = \frac{W_{air}}{W_{air} - W_{water}} \times \rho_{water}\ \left(\frac{gr}{cm^3}\right). \tag{3.2}$$

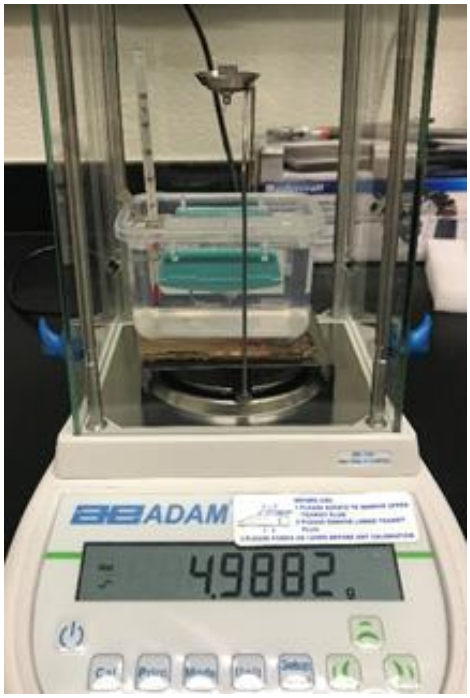

Figure 3.9 Archimedes setup for density measurement of sintered samples

3.5 SEM Imaging

3.5.1 Powder particles SEM imaging

Scanning Electron Microscopy (SEM) imaging of the powders was performed using the Vega3 SEM system (Tescan, Warrendale, PA). That SEM is a type of thermionic emission SEM system that comes from a heated tungsten filament as the electron sonurce. In order to qualitatively study the shape of powders, a quite thin layer of each powder adhered to a strip of crystal clear tape. Further, each tape that was covered by powders attached to a solid plastic slide and was put in the filmstrip holder. During imaging, casual areas were chosen over each slide and a sufficient number of pictures were taken from the powders. During the experiment, voltages of 15 kV and 20 kV were used for SEM imaging. SEM images from the powders were used to visually study their particle features such as their shape and satellite contents.

3.5.2 Sintered samples microstructure imaging

Prior to microstructure imaging of sintered samples, mounting, followed by polishing were done on them. The specimens were mounted in a conductive phenolic compound, ground, and polished for imaging of regions that were representative of the overall sample microstructure. Further, SEM was performed to study the microstructures of the samples after sintering. A special emphasis is placed on analyzing the precipitation of a sigma phase for the three materials. The SEM specimens were prepared using conventional metallography techniques and imaging was performed using Vega3 (Tescan, Warrendale, PA) equipped with Bruker XFLASH® energy dispersive spectroscopy (EDS) and backscattered electron (BSE) detectors.

Chapter 4

Results and Discussion

4.1 Results

4.1.1 Initial powder

The particle size distribution of the three 316L stainless steel powders is shown in Figure 4.1. The UMF powder in Figure 4.1(a) has a unimodal gaussian distribution with a size of 7 µm D10, 12 µm D50 and 18 µm D90. This PSD is commonly used in MIM process [110,111]. The BMC powder in Figure 4.1(b) has a non-discrete bimodal distribution with a size of 13 µm D10, 30 µm D50 and 50 µm D90. This PSD is typically used in PM process [112]. The BMF powder in Figure 4.1(c) has also non-discrete bimodal distribution with a particle size of 9 µm D10, 21 µm D50, and 40 µm D90. The SEM images in Figure 4.2 show the morphology of the as-received powders. All three powders have similar morphology, i.e. spherical or near-spherical, with some satellites. This dominant spherical morphology can improve powder flowability, packing density, and uniformity of the powder layer thickness. The true density of each powder, obtained through the gas pycnometry measurements, is given in Table 4.1. The three selected 316L powders, with similar morphologies, comparable densities and contrasting PSD, provide an excellent foundation for studying the effects of PSD on the sinterability of BJ printed samples.

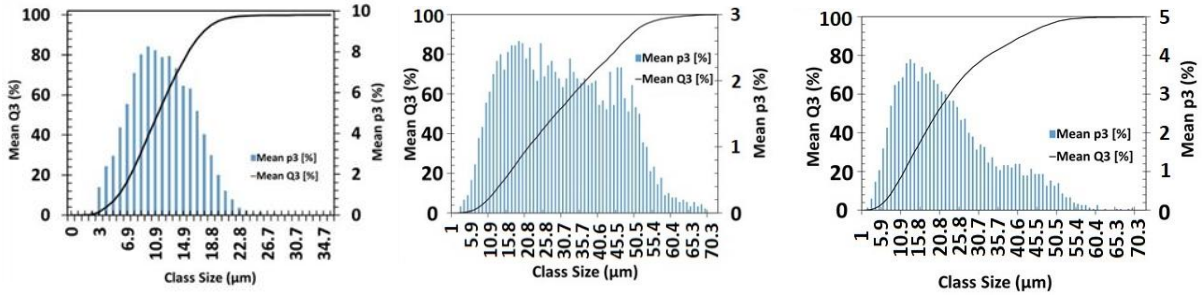

(a) (b) (c)

Figure 4.1: Particle size distribution graphs of (a) UMF, (b) BMC and (c) BMF stainless steel powders.

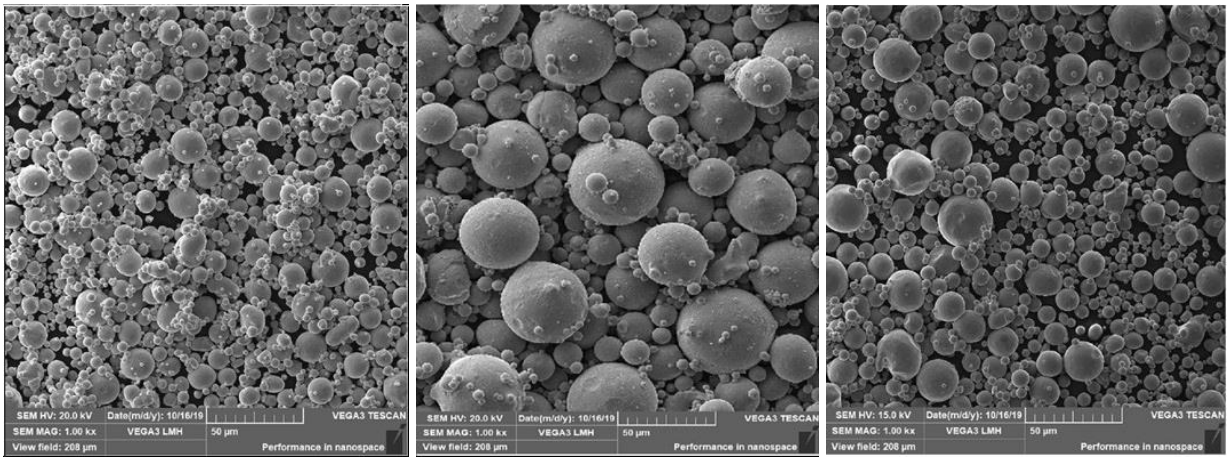

(a) (b) (c)

Figure 4.2: SEM images of (a) UMF, (b) BMC and (c) BMF stainless steel powders.

Table 4.1: The true densities of stainless steel powders obtained through gas pycnometry.

Powder name	Number of tests	Standard deviation (%)	Average density (g/cm^3)
UMF	15	0.011	7.8761
BMC	15	0.092	7.9651
BMF	15	0.057	7.9712

4.1.2 Thermogravimetric analysis

TGA is performed on GE binder to find the optimum debinding condition (Figure 4.3). According to the TGA curve, GE binder undergoes three decomposition steps. The first step occurs at a temperature range of 70 ^{o}C - 285 ^{o}C with a weight loss of 20 % which can be attributed to the loss of residual solvent and low molecular weight oligomer. The second step decomposition occurs at a temperature range of 285 ^{o}C - 420 ^{o}C with a weight loss of 43 % which can be attributed to the structural changes, such as loss of functional groups from polymer A. The third step decomposition occurs at a temperature range of 420 ^{o}C - 460 ^{o}C with a weight loss of 26 % which can be associated with degradation of the polymer backbone (or functional

groups from polymer B). Based on the tangent method, 285 ºC and 420 ºC found to be the inflection points of the curve and are selected as debinding temperatures to minimize the residual carbon content in the microstructure after sintering.

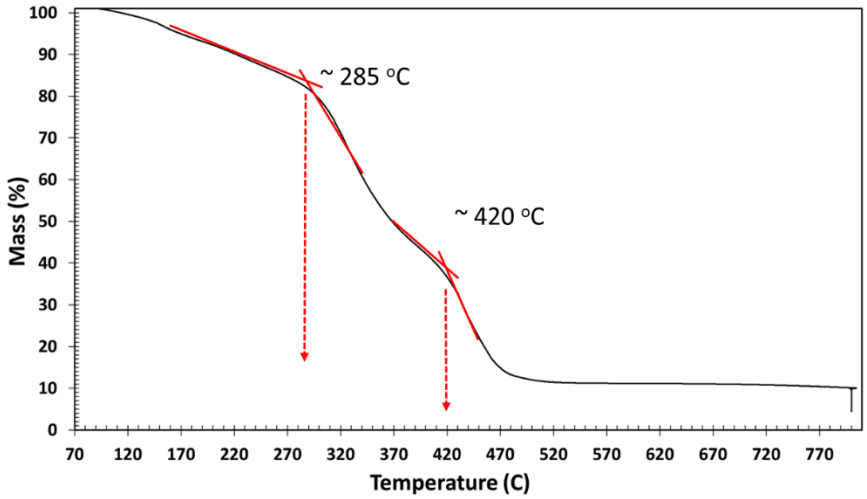

Figure 4.3: Thermal gravimetric analysis curve of GE polymeric binder.

4.1.3 Differential scanning calorimetry

Figure 4.4 shows the DSC results for all powders. It is observed that solidus and liquidus temperatures of DSC heating curves (Figure 4.4(a)) are different from those of DSC cooling curves (Figure 4.4(b)). This illustrates the effect of PSD on solidus and liquidus temperatures. UMF has the lowest solidus (1408 ºC) and liquidus (1450 ºC) temperatures on heating (Figure 4.4(a)) due to the less kinetic factors associated with the lowest median particle size (~ 12 µm). The fine particles have higher surface area inducing higher heat sensing. Thus, the resistance for solid to liquid transformation is reduced to a lower temperature [105]. As expected, coarser BMC and BMF have highest solidus (1418 ºC) and liquidus (1458 ºC) temperatures due to the pronounced kinetic factors. On the other hand, DSC cooling curves show that all three powders have almost the same solidus (~ 1402 ºC) and liquidus (~1434 ºC) temperatures. This is attributed to the phase change from liquid to solid which eliminates the kinetic factors associated with powder. The solidus and liquidus obtained from the heating and cooling curves are displayed in Table 4.2 Since sintering trials are done with isothermal holding at the

maximum temperature, the sintering temperatures are determined according to the cooling solidus temperature (~1402 ^{o}C) to guarantee subsolidus sintering.

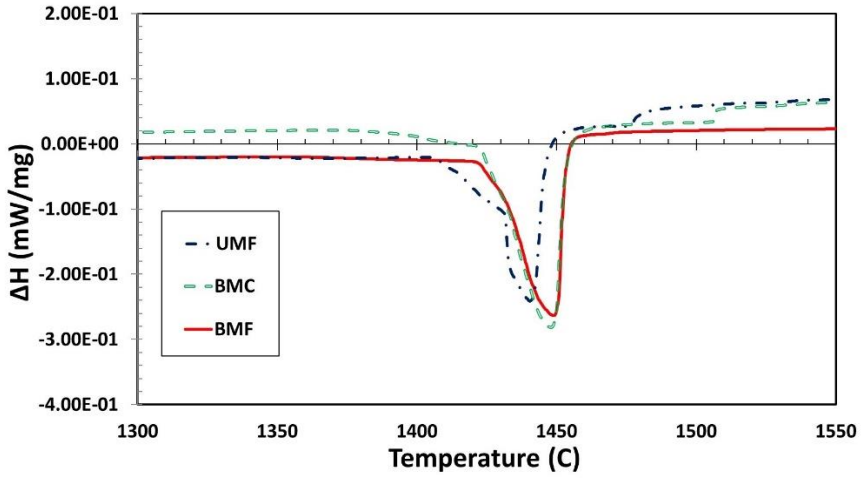

(a)

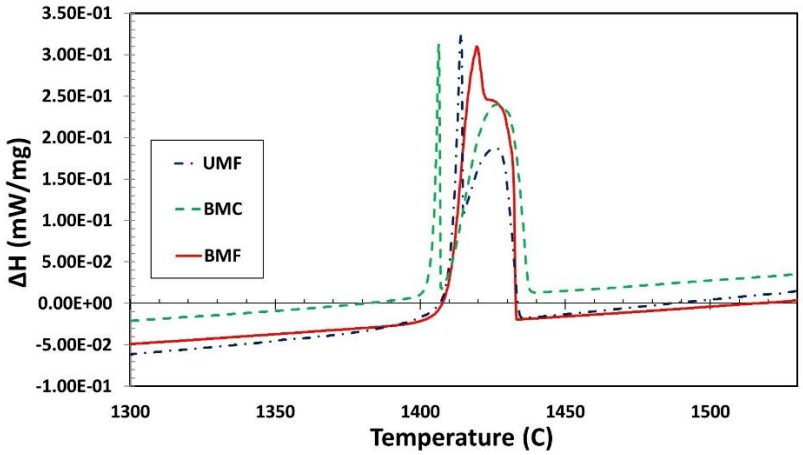

(b)

Figure 4.4: Differential scanning calorimetry curves of stainless steel powders during (a) heating and (b) cooling.

Table 4.2 Solidus and liquidus temperatures of stainless steel powders obtained from DSC.

	Solidus temperature (UMF)	Liquidus temperature (UMF)	Solidus temperature (BMC)	Liquidus temperature (BMC)	Solidus temperature (BMF)	Liquidus temperature (BMF)
Heating	1408°C	1450°C	1418°C	1458°C	1418°C	1458°C
Cooling	1402°C	1434°C	1400°C	1433°C	1403°C	1437°C

4.1.4 Powder sintering

4.1.4.1 Effect of PSD on sintering

The densification plots for the three powders with similar initial packing density are shown in Figure 4.5. The density is plotted versus the work of sintering described in Equation 2.7, where the temperature and time of the sintering are combined into one term (θ). Green samples were prepared carefully to get similar packing densities (65%) for all powders to decouple the effect of green density. The densification of the three powders exhibits a sigmoidal behavior. The UMF powder shows the sharp sintering curve and achieves the highest density (95%). This is because it has the lowest median particle size (12 µm D50). Small particles accelerate the densification due to higher surface energy [34,122]. In addition, smaller particles have larger contact area leading better diffusion between the particles [33]. Accordingly, The BMF (20 µm D50) and BMC powder (30 µm D50) achieved a lower density of 94% and 92%, respectively. Their sintering profiles also show shallower sintering slops due to their larger particle sizes.

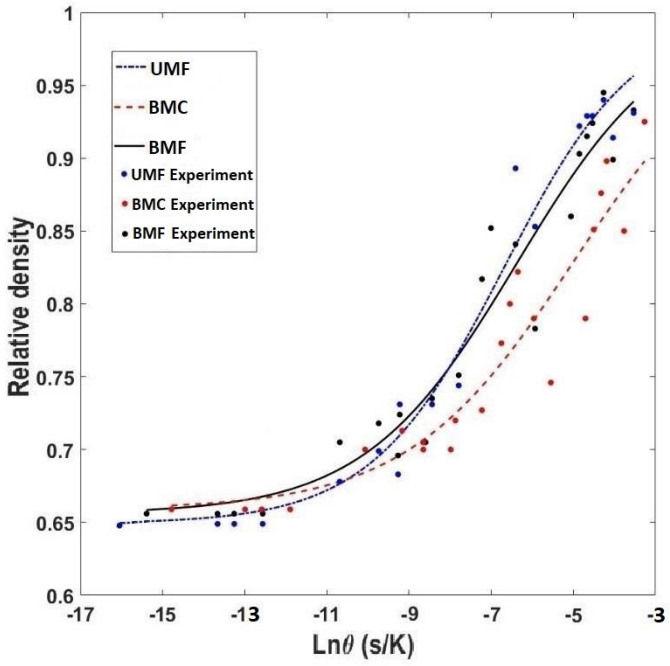

Figure 4.5: Master sintering curve for UMF, BMC and BMF powders with similar relative green density (65 %).

4.1.4.2 Effect of green density on sintering

Initial packing density is an important factor that influences the sinterability of BJ printed parts. Considering that the samples printed by BJ have relatively low green densities (50-60 %) [5], another set of samples with lower green densities were fabricated from BMC and BMF to replicate BJ samples in which the effect of PSD was decoupled. It should be noted that it was not possible to fabricate firm samples with lower green densities from UMF due to its undesirable rheology. Figure 4.6(a) shows the comparison between the densification behavior of high and low green density samples for BMF. The densification plots of both high and low green density samples exhibit a sigmoidal behavior and are plotted versus the work of sintering. From the Figure 4.6(a), low green density (LGD) samples with 58% relative green density reached the maximum density of 91% after sintering, whereas this value is 94% for high green density (HGD) samples with 65.4% relative green density. Similarly, Figure 4.6(b) compares high and low green density samples from BMC where the densification plots again show the density change versus the work of sintering and have a sigmoidal behavior. In the Figure 4.6(b), LGD

samples with 53% relative green density, achieved 78% after sintering, while the HGD samples with 65.6% relative green density attained 92%. Thus, in both BMF and BMC powders, the HGD samples always reached higher density after sintering due to the fact that higher green density increases the number of contact points per particle, known as the coordination number. Plus, higher green densities reduce pore sizes and enhance densification during the sintering because of the higher local stresses that enlarge the contact area between particles [34].

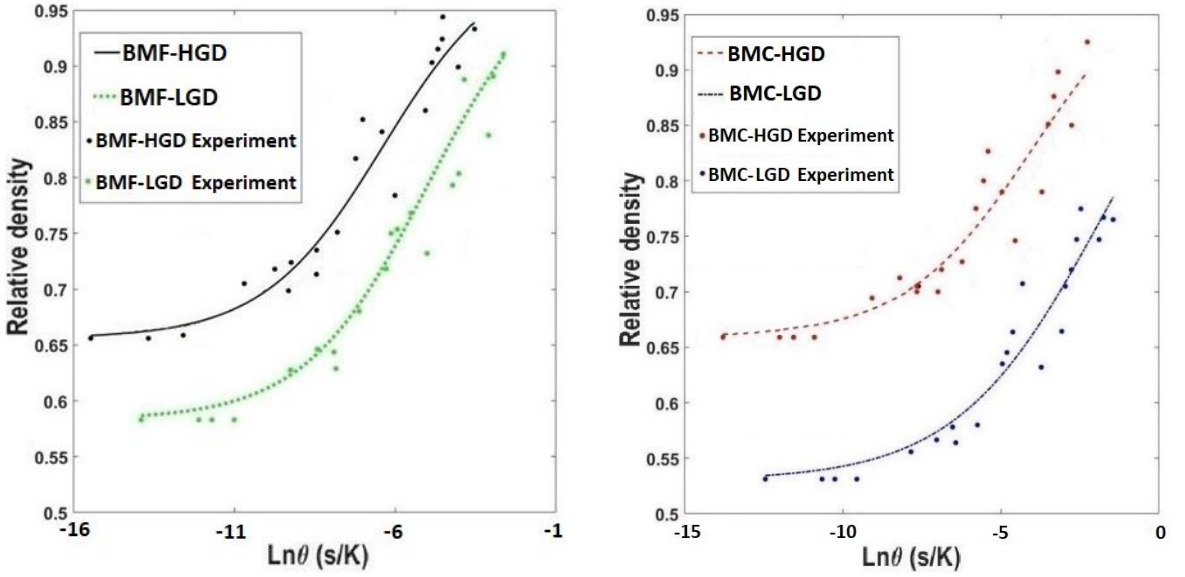

(a) (b)

Figure 4.6: Effects of green density on the master sintering curves for (a) BMC and (b) BMF powders

4.1.5 Sintering Microstructure

Microstructure observations reveal the formation of trangranular and intergranular Cr-Mo-rich phases for the samples with the highest density. Figure 4.7 shows the microstructure of BMF with 94% density. The Cr-Mo-rich phases also exhibit a depletion in Nickel. Selected area diffraction pattern (not shown here) confirms the particles to be sigma (σ) phase and carbide particles. Carbide particles are mostly spherical (Ø<10 μm) homogenously distributed in the microstructures. The σ phase a more elongated shape and is concentrated along the grain boundaries. The length of the sigma phase can easily exceed 10μm in length.

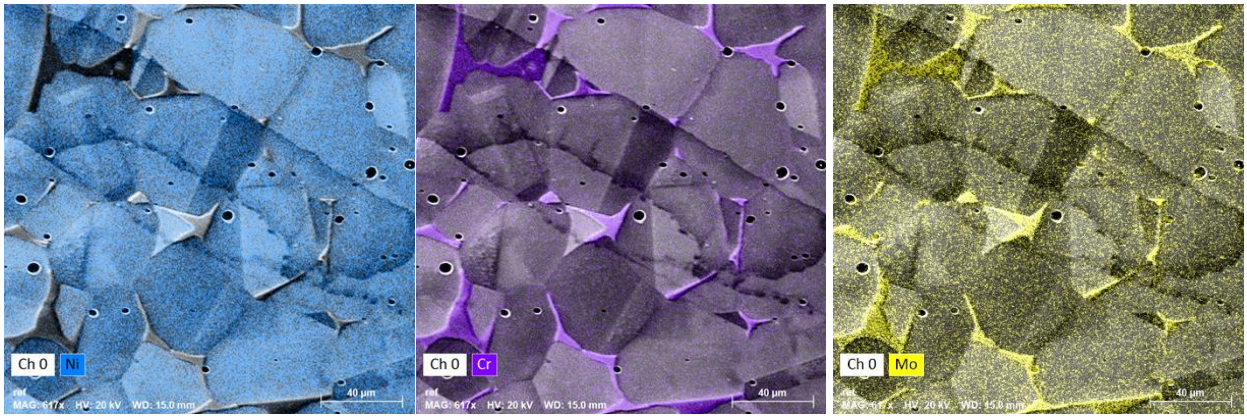

Figure 4.7: SEM BSE images with EDS chemical maps of BMF microstructure with initial relative green density of 65 % after sintering at 1400 °C for 600 minutes.

4.2 Discussion

Based on the results from Figure 4.5, PSD of the powders has a small effect on the maximum sintered density. The samples prepared from UMF, BMF, and BMC with similar high green densities (~65%) showed small differences in their maximum sintered densities from 92% to 95%. On the other hand, from Fig. 7a and b, it is observed that the initial packing density plays a much more important role in the densification of the green samples. The samples with lower green densities of 53% and 58%, reached noticeably lower sintered densities of 78% and 91%, respectively. To obtain a better understanding of the difference in the densification behavior, the MSC analytical model was implemented and the experimental data were fitted to a sigmoidal curve through the non-linear regression curve fitting method.

4.2.1 Master sintering curves

The density of sintered samples was measured and analyzed by considering the solid-state sintering theory [83,85]. The solid-state sintering involves three major diffusion mechanisms associated with different activation energies. Since these mechanisms working in cooperation, it is difficult to determine their contribution and the temperature they get activated during the sintering cycle. Generally, to ease the analysis, an equal activation energy value for the entire sintering cycle is considered, which is called apparent activation energy. In this work, the

apparent activation energy for each powder was determined by minimizing the residuals between the experimental data and the predicted data from the MSC model (Equation 2.9). The procedure to find the apparent activation energy was conducted through iteration and comprehensively described in section 2.4.1, Equation 2.8, of this thesis.

The MSC fits for the three powders with high green densities are shown in Figure 4.5, while the two powders with low green densities are shown in Figure 4.6. The normal probability plots for all five MSC fits are presented in Figure 4.8. It compares the residual errors of experimental and predicted data from non-linear regression. It shows that the residuals of all five MSC are normally distributed presenting a P-value higher than 0.05.

The statistical accuracy of the five MSC fits is presented in Table 4.3. The coefficient of determination, also called R-square, is higher than 90% for all five MSC fits. The root mean square error (RMSE) showing the standard deviation of the residuals and how they are spread out in the MSC are relatively low (<0.028). Finally, standard error (SE) of predicted constants *b* and *c* in Equation 2.9 are also given in Table 4.3.

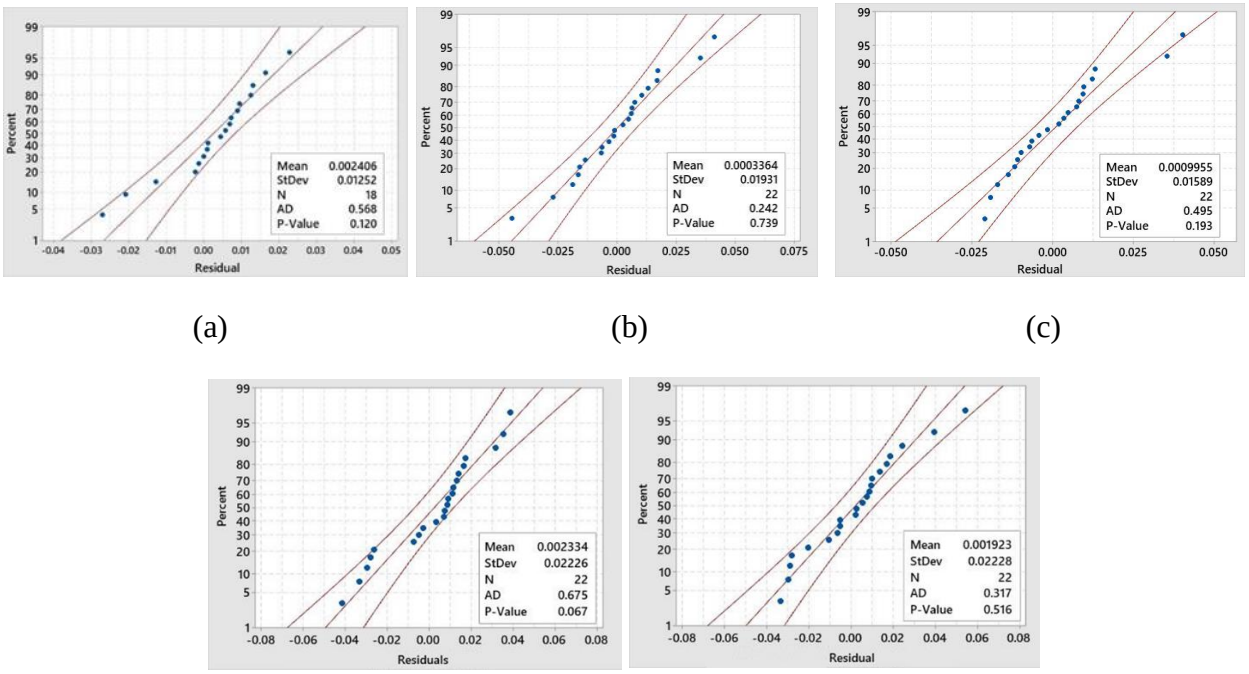

(a) (b) (c)

(d) (e)

Figure 4.8: Normal probability plot for (a) UMF, (b) BMC-HGD, (c) BMF-HGD, (d) BMF-LGD and (e) BMC-LGD.

Table 4.3 Nonlinear regression summary statistics.

	R-square (%)	RMSE	SE (b)	SE (c)
UMF	97.4	0.020	0.15	0.13
BMC-HGD	91.5	0.025	0.20	0.23
BMF-HGD	94	0.028	0.21	0.23
BMC-LGD	92.3	0.024	0.19	0.22
BMF-LGD	90.5	0.037	0.19	0.23

4.2.1.1 Activation energy

The residuals for the MSC associated with the three powders in Figure 4.5 and the two green densities in Figure 4.6 were computed for a range of Q and are shown in Figure 4.9. The apparent activation energy resulting in the lowest residual for the 5 MSC fits range between 103 and 110 kJ/mol. From previous works, R. M. German [95] studied the solid-state sintering of 316L powder and apparent activation energy was reported around 167 kJ/mol. The slight deviation in activation energies between this work and R. M. German can be attributed to difference of the powder preparation technique (water atomized powder), sample preparation technique (injection molding) and binder composition. Previous studies indicate that powder particle size, powder morphology, binder composition, green part density, debinding and sintering conditions affect the sintering behavior and the diffusion phenomena and hence the value of apparent activation energy [34,113–115].

The volume fraction of ferrite in the microstructure can also reduce the activation energy for sintering. Wu et al. showed that the sintering density increases with the volume fraction of ferrite in the microstructure [116]. This is because the diffusion rate is higher in ferrite than austenite. The high-volume fraction of σ-phase in Figure 4.7 means that a high-volume fraction of δ-ferrite is present during the sintering of the material. The Cr-rich δ-ferrite decomposes into the σ-phase during the slow cooling of the material [117]. This means that the activation energy is capturing both the contribution of the austenite and the ferrite in the solid-state sintering.

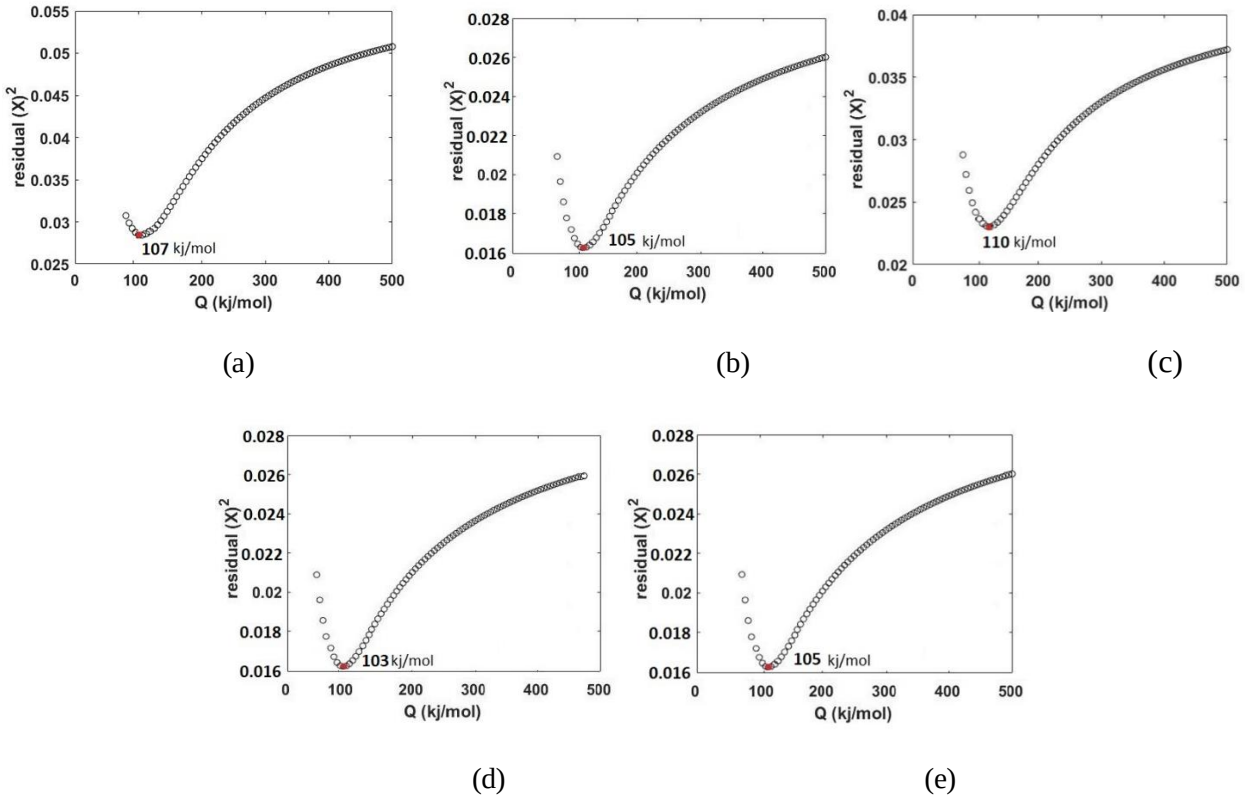

Figure 4.9: Determination of apparent activation energy for (a) UMF, (b) BMC-HGD, (c) BMF-HGD, (d) BMF-LGD and (e) BMC-LGD.

4.2.1.2 Onset of sintering

The onset of sintering values in Figure 4.10. are obtained from the first and second derivatives of master sintering curves. Table 4.4 summarizes the difference in onsets of sintering for the three powders with different PSD and two green densities. For the same green density (~ 65 %), UMF has 7 % and 12.2 % lower ln(θ) value than that of BMF and BMC, respectively. This shows that reducing the PSD expediates the onset of sintering which can be attributed to the lower median particle size of UMF powder providing more particle-particle contacts within the sample. In addition, as particles get smaller, they have more surface energy. This makes sintering favorable and requires less work to initiate the densification [33].

On the other hand, the green density has a more noticeable impact on the onset of sintering (Table 4.4). BMF-LGD has 10 % higher work of sintering than that of BMF-HGD. Similarly, BMC-LGD has 17.5 % higher work of sintering than that of BMC-HGD. This illustrates that

increasing the green density facilitates the onset of sintering significantly. From the microscale point of view, this can be attributed to the increase in the number of contacts within the powder particles as porosity and pore size reduces in the green sample. During sintering, these contact areas enlarge owing to local stresses at these points, leading the formation of more necks and eventually more grain boundaries accompanied with shorter diffusion paths. All these factors reduce the amount of work of sintering to initiate the densification [34,118].

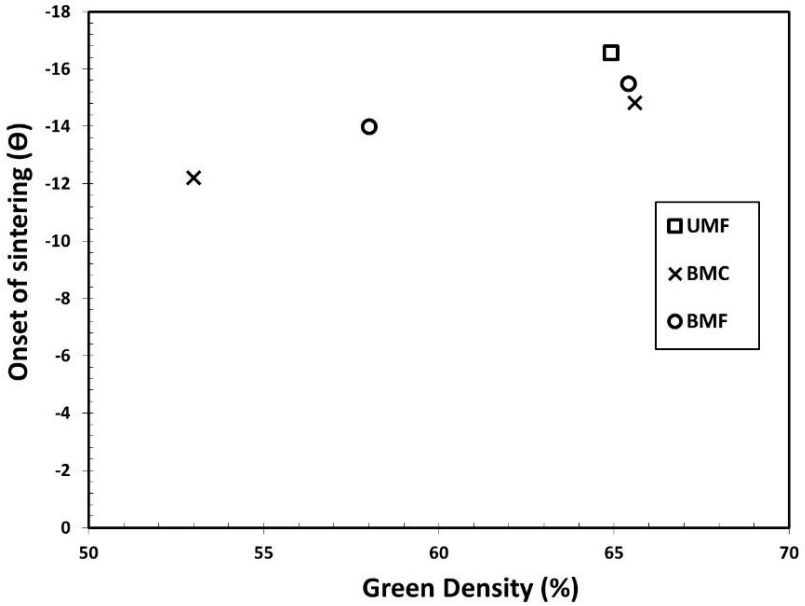

Figure 4.10: Onset work of sintering (Θ) values for UMF, BMC and BMF plotted against green density.

Table 4.4. Summary of differences in onset of sintering and densification rate.

	Difference in onset of sintering (%)		Difference in densification rate (%)	
	BMC-HGD	BMF-HGD	BMC-HGD	BMF-HGD
UMF	-12.2	-7	+15	+4.5
BMC-LGD	+17.5	NA	-5	NA
BMF-LGD	NA	+10	NA	-6.8

4.2.1.3 Densification rate

The densification rates in Figure 4.11 are obtained from the slope of the master sintering curves. Table 4.4 summarizes the differences in the densification rates for the three powders with different PSD and two green densities. The slope of sintering at 65 % green density for UMF is 4.5 % and 15 % larger than that of BMF and BMC, respectively. As expected, for the same green density, decreasing the PSD enhanced the densification kinetics. This is due to the higher surface energy of finer particles which has stronger driving force for sintering to consume the surface energy. For the same PSD, it is observed that increasing the green density also accelerates the densification. As shown in Figure 4.11, BMF and BMC at lower green densities exhibited 6.8% and 5% lower densification rates, respectively, compared to their higher green densities. This can be attributed to the maximized number of particle contacts leading the formation of many grain boundaries and short diffusion paths, both favoring faster sintering [34,119].

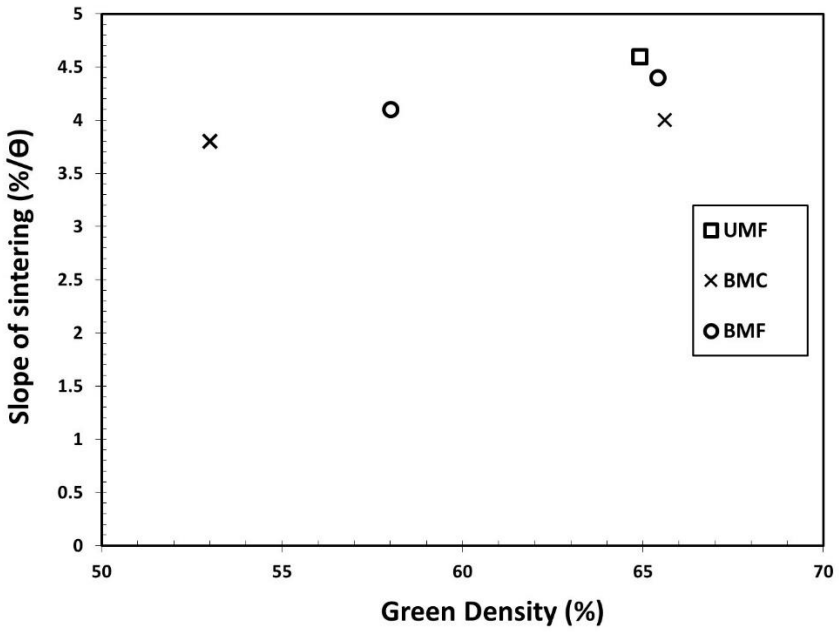

Figure 4.11: Slope of sintering values for UMF, BMC and BMF plotted against green density.

4.2.2 Flowability

As a powder bed AM technology, BJ requires a powder material withdesirable flowability. In that regard, in order to examine the processability of a powder, the flowability test should be

done to characterize the ability of a powder to compact well and reach a high green density for any type of powder bed AM technology. Otherwise, powder material cannot be spread smoothly and uniformly onto the bed and leads to structural defects in the part during the printing step [12,22,120]. Figure 4.12 shows the total stability energy of powder materials versus the flow rate. This figure is used to build Table 4.5 presenting the powder flowability factors. Based on the specific energy (SE) factor, UMF has the highest specific stability energy corresponding to the lowest flowability. Also, from the stability index (SI) factor which represents how much powder is stable in terms of flowability at different flow rates, BMF is the most stable powder, while UMF is the least stable powder. It should be noted that the closer the SI value to 1, the more stable the powder. The difference in the flowability of the powders is related to their particle size. In fact, powders with large particles have suitable flowability due to low interparticle friction and weak van der Waals forces while powders with smaller particle size tend to agglomerate and have poor flowability because of the electrostatic forces between small particles [12,22,27-28,30]. Based on the flowability test, UMF is not qualified to be used for the BJ process. BMF and BMC have good flowability based on SE factor but BMF is more stable at different flow rates which makes it a superior candidate to be used in BJ.

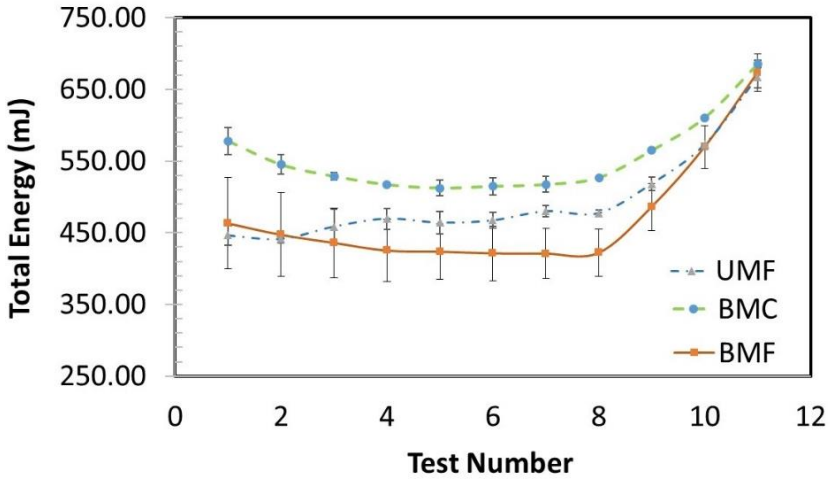

Figure 4.12: Energy consumption during dynamic flow of UMF, BMC and BMF powders.

Table 4.5 Flow properties for UMF, BMC and BMF powders.

Powder name	Number of tests	Specific energy (mJ/g)	Stability index
UMF	11	4.92	1.09
BMC	11	2.66	0.93
BMF	11	2.85	0.98

4.2.3 Sintered microstructures

The current investigation on 316L powders shows that the sintering temperature and time must be above 1200°C for more than 1 hour in order to obtain a minimum relative density of 90%. The precipitation kinetic of σ-phase is strongly dependent on the alloy composition [117]. The nose of the TTT curve is located at a temperature range of 800°C~850°C. The incubation time for precipitation varies strongly with the alloy composition. Perron et al. showed that a slight addition on Nb in 316L alloy can reduce the incubation time for σ-phase precipitation below 1 minute [121]. It is thus not surprising to observe a high density of σ-phase in the sintering microstructure in Figure 4.7.

The precipitation of σ-phase particles has a detrimental effect on the properties of 316L alloy [117]. On the one hand, it leads to a depleted zone in the surrounding γ matrix (see Figure 4.7). The *σ*-phase and *γ*-austenite induce the galvanic effect, and the *γ*-austenite is corroded preferentially. Consequently, the corrosion potent is decreased. On the other hand, σ-phase also leads to brittle regions which reduce the ductility of the material. In order to reduce the amount of σ-phase in the final microstructure, a solutionizing heat treatment was applied to the sintering microstructure shown in Figure 4.7. The microstructure was heat treated to 1050°C for 30 minutes then air cooled. Figure 4.13 shows that heat treatment dissolved entirely the σ-phase. The Cr-rich carbides are the only precipitates that remain in the microstructure.

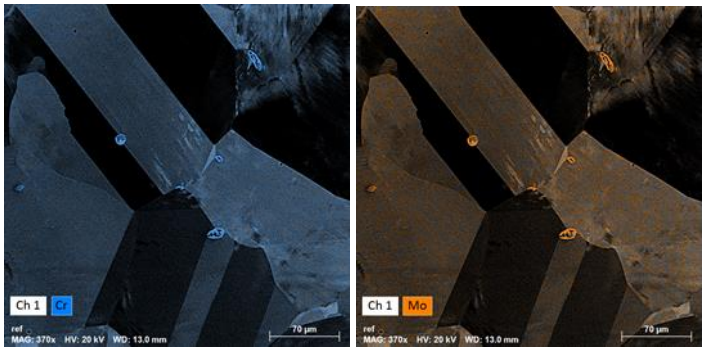

Figure 4.13: SEM BSE images with EDS chemical maps of BMF microstructure with initial relative green density of 65 % after sintering at 1400°C for 600 minutes followed by solutionizing at 1050°C for 30 minutes.

Chapter 5

Conclusions & Future Work

5.1 Conclusions

This thesis focuses on defining the important criteria to select powder for BJ additive manufacturing applications. It evaluates the effect of PSD and green density on the sinterability of the BJ samples. In order to decouple these two parameters, green samples were fabricated in a controlled environment. A total of 280 samples were prepared in the laboratory. Three different PSD and three green densities were evaluated. Debinding and sintering treatments were applied to the green samples and their relative densities measured using the Archimedes method. Here are the major conclusions obtained from this study:

5.1.1 Heat-treatment analysis

The polymeric binder used for this work was provided by GE. The thermal gravimetric analysis shows two decomposition stages. This is because the binder is made of two polymers. The first decomposition stage initiates around 285°C and the second stage around 420°C. These two temperatures were chosen to design the optimum de-binding conditions.

Differential scanning calorimetry analysis of the three powders shows a slight change in solidus and liquidus temperatures during heating. The finer (UMF) powder has the lowest solidus (1408°C) and liquidus (1450°C), while the coarser (BMC) powder has the highest solidus (1418°C) and liquidus (1458°C). The fine particles have higher surface area inducing higher heat sensing. Thus, the resistance for solid to liquid transformation is reduced to a lower temperature. DSC analysis during cooling shows that all three powders have almost the same solidus (~ 1402 oC) and liquidus (~1434 oC) temperatures. This is attributed to the phase change from liquid to solid which eliminates the kinetic factors associated with powder.

All the sintering temperatures are below 1400°C to guarantee sub-solidus sintering. Analysis of the microstructure and the activation energy confirmed that sintering occurred through solid state

diffusions in austenite and δ-ferrite. The three PSD and range of green densities investigated here did not affect the sintering mechanism.

The sintering microstructure has a high volume fraction of detrimental σ-phase. This is due to the high sintering temperatures (>900°C) and a long time (>30 minutes) employed. The σ-phase precipitates can be solutionized using a short heat treatment above 1000°C.

5.1.2 Densification data and Master Sintering Curve

All the sintering data follow a sigmoidal shape and MSC fit is utilized to describe analytically the sintering behavior. Statistical analysis showed that all the MSC fits have a R-square value higher than 90% with a normal distribution of their residuals.

The MSC theory is used to analyze the sintering kinetics of the three powders and the different green densities. While the PSD and green density does not affect the sintering mechanism, they have a strong impact on the sintering kinetics.

The finer powder (UMF) has the lowest work required to initiate sintering. It also has the fastest sintering rate and thus the highest final density (95 %). The coarser powder (BMC) requires more work to trigger sintering. The densification rate is also significantly slower leading to the lowest relative density (92 %).

The green density has a stronger impact on the sintering kinetics. The work required to trigger sintering is increased by 17.5 % when the green density is reduced from 65% to 53%. This is much higher than what is observed when the PSD is modified. As a reference, the difference in the onset of sintering for the UMC and BMC is only 12.2%. Decreasing the green density also reduces the densification rate and leads to a much lower final density.

The results presented in this investigation shows that the PSD is important to optimize the relative density of a BJ additive manufacturing printed parts. However, the green density has a much stronger impact on the final density. Thus, the capacity of the powder to flow and compact in the powder bed must be the first criterion for powder selection. The flowability tests performed on the three powders show that it is the BMF that behaves the best.

5.2 Future works

The approach derived in this thesis provides a foundation for more progress in studying BJ process improvement. Improvements can be defined in terms of experimental, analytical, and numerical studies.

In order to improve the accuracy of the analytical model obtained from the MSC theory, dilatometry measurements are recommended to be conducted in future work to accomplish and compare with the results of this thesis. Also, it is recommended to conduct the TGA test on printed samples in order to investigate the debinding of a real BJ product as well as the interaction of powder and binder.

As the shrinkage is an unattachable feature of sintering, studies on predicting shrinkage as well as shape distortion of BJ products are of interest.

Another important aspect of this thesis, which would be interesting to study as future work, is linking the analytical sintering densification model obtained from MSC theory to a FEM model to predict mechanical and geometrical part properties. A UMAT code should be generated for that purpose and it needs to be done to expand the application of the MSCs more than predicting the density.

Mechanical properties improvement is of interest and in that regard, mechanical testing should be conducted and the results will need to compare with microstructure analysis, grain size, and porosity distribution to enhance mechanical properties.

Last but not least, the printing and sintering of complex industrial-scale products are of interest. Stainless steel powder materials, particularly 316L grade have a great application in manufacturing automotive parts hence studying the densification behavior of industrial-scale BJ printed parts would be a practical extension to this thesis in the future.

References:

1. Herzog, D., Seyda, V., Wycisk, E., & Emmelmann, C. (2016). Additive manufacturing of metals. Acta Materialia, 117, 371–392.
2. Bernhard, M. (2012). Additive Manufacturing Technologies – Rapid Prototyping to Direct Digital Manufacturing. Assembly Automation, 32(2).
3. Do, T., Kwon, P., & Shin, C. S. (2017). Process development toward full-density stainless steel parts with binder jetting printing. International Journal of Machine Tools and Manufacture, 121, 50–60.
4. DebRoy, T., Wei, H. L., Zuback, J. S., Mukherjee, T., Elmer, J. W., Milewski, J. O., Zhang, W. (2018). Additive manufacturing of metallic components–process, structure and properties. Progress in Materials Science, 92, 112–224.
5. Mirzababaei, S., & Pasebani, S. (2019). A Review on Binder Jet Additive Manufacturing of 316L Stainless Steel. Journal of Manufacturing and Materials Processing, 3(3), 82.
6. Frazier, W. E. (2014). Metal Additive Manufacturing: A Review. Journal of Materials Engineering and Performance, 23(6), 1917–1928.
7. Conner, B. P., Manogharan, G. P., Martof, A. N., Rodomsky, L. M., Rodomsky, C. M., Jordan, D. C., & Limperos, J. W. (2014). Making sense of 3-D printing: Creating a map of additive manufacturing products and services. Additive Manufacturing, 1–4, 64–76.
8. Stucker, B. Additive manufacturing technologies: Technology introduction and business implications. In Frontiers of Engineering: Reports on Leading-Edge Engineering from the 2011 Symposium; National Academies Press: Washington, DC, USA, 2012; pp. 19–21.
9. Gokuldoss, P. K., Kolla, S., & Eckert, J. (2017). Additive manufacturing processes: Selective laser melting, electron beam melting and binder jetting—Selection guidelines. Materials, 10(6), 672.
10. Chen, H., & Zhao, Y. F. (2016). Process parameters optimization for improving surface quality and manufacturing accuracy of binder jetting additive manufacturing process. Rapid Prototyping Journal.
11. Gibson, I.; Rosen, D.; Stucker, B. Binder Jetting. In Additive Manufacturing Technologies: 3D Printing, Rapid Prototyping, and Direct Digital Manufacturing; Springer: New York, NY, USA, 2015; pp. 205–218.

12. Utela, B., Storti, D., Anderson, R., & Ganter, M. (2008). A review of process development steps for new material systems in three dimensional printing (3DP). Journal of Manufacturing Processes, 10(2), 96–104.
13. Li, M., Du, W., Elwany, A., Pei, Z., & Ma, C. (n.d.). Binder Jetting Additive Manufacturing of Metals: A Literature Review. ASME 2019 14th International Manufacturing Science and Engineering Conference. American Society of Mechanical Engineers Digital Collection.
14. Du, W., Ren, X., Ma, C., & Pei, Z. (2017). Binder jetting additive manufacturing of ceramics: a literature review. ASME 2017 International Mechanical Engineering Congress and Exposition. American Society of Mechanical Engineers Digital Collection.
15. Dini, F., Ghaffari, S. A., Jafar, J., Hamidreza, R., & Marjan, S. (2019). A review of binder jet process parameters; powder, binder, printing and sintering condition. Metal Powder Report.
16. Lores, A., Azurmendi, N., Agote, I., & Zuza, E. (2019). A review on recent developments in binder jetting metal additive manufacturing: materials and process characteristics. Powder Metallurgy, 62(5), 267–296.
17. Boris Hein S, Aumund-Kopp C, Barthel B. Binder Jet metal AM: process chain considerations when moving towards series production. Met Addit Manuf. 2018;4 (4):79–85.
18. Vlasea, M., Toyserkani, E., & Pilliar, R. (2015). Effect of gray scale binder levels on additive manufacturing of porous scaffolds with heterogeneous properties. International Journal of Applied Ceramic Technology, 12(1), 62–70.
19. Ghaffar, S. H., Corker, J., & Fan, M. (2018). Additive manufacturing technology and its implementation in construction as an eco-innovative solution. Automation in Construction, 93, 1–11.
20. Mostafaei, A., Stevens, E. L., Hughes, E. T., Biery, S. D., Hilla, C., & Chmielus, M. (2016). Powder bed binder jet printed alloy 625: Densification, microstructure and mechanical properties. Materials & Design, 108, 126–135.
21. Three Dimensional Printing. Available online: http://www.mit.edu/~{}tdp/index.html
22. Lv, X., Ye, F., Cheng, L., Fan, S., & Liu, Y. (2019). Binder jetting of ceramics: Powders, binders, printing parameters, equipment, and post-treatment. Ceramics International.

23. Butscher, A., Bohner, M., Roth, C., Ernstberger, A., Heuberger, R., Doebelin, N., … Müller, R. (2012). Printability of calcium phosphate powders for three-dimensional printing of tissue engineering scaffolds. Acta Biomaterialia, 8(1), 373–385.
24. Bai, Y., & Williams, C. B. (2015). An exploration of binder jetting of copper. Rapid Prototyping Journal.
25. E. Wheat. Process Mapping and Optimization of Titanium Parts Made by Binder Jetting Additive Manufacturing, 2018.
26. Bai, Y., Wagner, G., & Williams, C. B. (2017). Effect of Particle Size Distribution on Powder Packing and Sintering in Binder Jetting Additive Manufacturing of Metals. Journal of Manufacturing Science and Engineering, 139(8).
27. Upadhyaya, G. S. (2006). German RM, Powder metallurgy and particulate materials processing, Metal powder industries federation, Princeton, USA, 2005, pp. 522, isbn 0-9762057-1-8. Science of Sintering, 38(1), 95.
28. Ziaee, M., & Crane, N. B. (2019). Binder jetting: A review of process, materials, and methods. Additive Manufacturing.
29. Matsusaka, S., Maruyama, H., Matsuyama, T., & Ghadiri, M. (2010). Triboelectric charging of powders: A review. Chemical Engineering Science, 65(22), 5781–5807.
30. Castellanos, A. (2005). The relationship between attractive interparticle forces and bulk behaviour in dry and uncharged fine powders. Advances in Physics, 54(4), 263–376.
31. Wang, Y., & Zhao, Y. F. (2017). Investigation of sintering shrinkage in binder jetting additive manufacturing process. Procedia Manufacturing, 10, 779–790.
32. Zheng, J., Carlson, W. B., & Reed, J. S. (1995). The packing density of binary powder mixtures. Journal of the European Ceramic Society, 15(5), 479–483.
33. Park, D. Y., Lee, S. W., Park, S. J., Kwon, Y.-S., & Otsuka, I. (2013). Effects of particle sizes on sintering behavior of 316L stainless steel powder. Metallurgical and Materials Transactions A, 44(3), 1508–1518.
34. German, R. (2014). Sintering: from empirical observations to scientific principles. Butterworth-Heinemann.
35. Li, R., Shi, Y., Wang, Z., Wang, L., Liu, J., & Jiang, W. (2010). Densification behavior of gas and water atomized 316L stainless steel powder during selective laser melting. Applied Surface Science, 256(13), 4350–4356.

36. Ederer, L. The Effect of Zinc Stearate on the Compaction and Sintering Characteristics of a Ti-6% A1-4% V Hydride-Dehydride Powder; McGill University Libraries: Burnaby, BC, Canada, 1999.
37. Bai, Y., & Williams, C. B. (2018). Binder jetting additive manufacturing with a particle-free metal ink as a binder precursor. Materials & Design, 147, 146–156.
38. FRYKHOLM, R., TAKEDA, Y., ANDERSSON, B.-G., & CARLSTRÖM, R. (2016). Solid state sintered 3-D printing component by using inkjet (binder) method. Journal of the Japan Society of Powder and Powder Metallurgy, 63(7), 421–426.
39. Juan, H.L. Effect of Temperature Ratio (ts/tm) and Time on the Sintering Behavior of Metallic 316l Stainless Steel Coupons Coupons Produced Using Jet-Binder Technology. Master's Thesis, University of Pittsburgh, Pittsburgh, PA, USA, 2017.
40. Mostafaei, A., Behnamian, Y., Krimer, Y. L., Stevens, E. L., Luo, J. L., & Chmielus, M. (2016). Effect of solutionizing and aging on the microstructure and mechanical properties of powder bed binder jet printed nickel-based superalloy 625. Materials & Design, 111, 482–491.
41. Do, T., Bauder, T. J., Suen, H., Rego, K., Yeom, J., & Kwon, P. (2018). Additively Manufactured Full-Density Stainless Steel 316L with Binder Jet Printing. ASME 2018 13th International Manufacturing Science and Engineering Conference. American Society of Mechanical Engineers Digital Collection.
42. Doyle, M., Agarwal, K., Sealy, W., & Schull, K. (2015). Effect of layer thickness and orientation on mechanical behavior of binder jet stainless steel 420+ bronze parts. Procedia Manufacturing, 1, 251–262.
43. Vlasea, M., Pilliar, R., & Toyserkani, E. (2015). Control of Structural and Mechanical Properties in Bioceramic Bone Substitutes via Additive Manufacturing Layer Stacking Orientation. Additive Manufacturing, 6.
44. Asadi-Eydivand, M., Solati-Hashjin, M., Farzad, A., & Osman, N. A. A. (2016). Effect of technical parameters on porous structure and strength of 3D printed calcium sulfate prototypes. Robotics and Computer-Integrated Manufacturing, 37, 57–67.
45. Atre, S., Porter, J., Batchelor, T., Bulger, K. K. M., & Gangopadhya, P. (2016). Process parameter optimization for binder jetting using 420 stainless steel. European Congress

and Exhibition on Powder Metallurgy. European PM Conference Proceedings, 1–6. The European Powder Metallurgy Association.

46. Gonzalez, J. A., Mireles, J., Lin, Y., & Wicker, R. B. (2016). Characterization of ceramic components fabricated using binder jetting additive manufacturing technology. Ceramics International, 42(9), 10559–10564.
47. Gregorski, S. J. (2003). High green density metal parts by vibrational compaction of dry powder in the three-dimensional printing process.
48. Miyanaji, H., Momenzadeh, N., & Yang, L. (2018). Effect of printing speed on quality of printed parts in Binder Jetting Process. Additive Manufacturing, 20, 1–10.
49. Miyanaji, H., Zhang, S., & Yang, L. (2018). A new physics-based model for equilibrium saturation determination in binder jetting additive manufacturing process. International Journal of Machine Tools and Manufacture, 124, 1–11.
50. Shrestha, S., & Manogharan, G. (2017). Optimization of binder jetting using Taguchi method. Jom, 69(3), 491–497.
51. Hsu, T., & Lai, W. (2010). Manufacturing parts optimization in the three-dimensional printing process by the Taguchi method. Journal of the Chinese Institute of Engineers, 33(1), 121–130.
52. Parab, N. D., Barnes, J. E., Zhao, C., Cunningham, R. W., Fezzaa, K., Rollett, A. D., & Sun, T. (2019). Real time observation of binder jetting printing process using high-speed X-ray imaging. Scientific Reports, 9(1), 2499.
53. Moon, J., Grau, J. E., Knezevic, V., Cima, M. J., & Sachs, E. M. (2002). Ink-jet printing of binders for ceramic components. Journal of the American Ceramic Society, 85(4), 755–762.
54. Shirazi, S. F. S., Gharehkhani, S., Mehrali, M., Yarmand, H., Metselaar, H. S. C., Kadri, N. A., & Osman, N. A. A. (2015). A review on powder-based additive manufacturing for tissue engineering: selective laser sintering and inkjet 3D printing. Science and Technology of Advanced Materials, 16(3), 33502.
55. Heaney, D. F. (2018). Handbook of metal injection molding. Woodhead Publishing.
56. Simchi, A., Rota, A., & Imgrund, P. (2006). An investigation on the sintering behavior of 316L and 17-4PH stainless steel powders for graded composites. Materials Science and Engineering: A, 424(1–2), 282–289.

57. Mariappan, R., Kumaran, S., & Rao, T. S. (2009). Effect of sintering atmosphere on structure and properties of austeno-ferritic stainless steels. Materials Science and Engineering: A, 517(1–2), 328–333.
58. Mostafaei, A., Toman, J., Stevens, E. L., Hughes, E. T., Krimer, Y. L., & Chmielus, M. (2017). Microstructural evolution and mechanical properties of differently heat-treated binder jet printed samples from gas-and water-atomized alloy 625 powders. Acta Materialia, 124, 280–289.
59. Gutmanas, E. Y. (1980). High-pressure compaction and cold sintering of stainless steel powders. Powder Metallurgy International, 12(4), 178–183.
60. Rishmawi, I., Salarian, M., & Vlasea, M. (2018). Tailoring green and sintered density of pure iron parts using binder jetting additive manufacturing. Additive Manufacturing, 24, 508–520.
61. M. Vlasea. Additive Manufacturing Methodology and System for Fabrication of Porous Structures with Functionally Graded Properties, 2014.
62. Basalah, A., Esmaeili, S., & Toyserkani, E. (2016). On the influence of sintering protocols and layer thickness on the physical and mechanical properties of additive manufactured titanium porous bio-structures. Journal of Materials Processing Technology, 238, 341–351.
63. Ziaee, M., Tridas, E. M., & Crane, N. B. (2017). Binder-jet printing of fine stainless steel powder with varied final density. Jom, 69(3), 592–596.
64. Bourell, D., Kruth, J. P., Leu, M., Levy, G., Rosen, D., Beese, A. M., & Clare, A. (2017). Materials for additive manufacturing. CIRP Annals, 66(2), 659–681.
65. A. Bailey, A. Merriman, A. Elliott, and M. Basti. Preliminary Testing of Nanoparticle Effectiveness in Binder Jetting Applications. 27th Annual International Solid Freeform Fabrication Symposium, pages 1069{1077, 2016.
66. Cordero, Z. C., Siddel, D. H., Peter, W. H., & Elliott, A. M. (2017). Strengthening of ferrous binder jet 3D printed components through bronze infiltration. Additive Manufacturing, 15, 87–92.
67. Kumar, A., Bai, Y., Eklund, A., & Williams, C. B. (2017). Effects of hot isostatic pressing on copper parts fabricated via binder jetting. Procedia Manufacturing, 10, 935–944.

68. Yang, L., Hsu, K., Baughman, B., Godfrey, D., Medina, F., Menon, M., & Wiener, S. (2017). Additive manufacturing of metals: the technology, materials, design and production. Springer.
69. Muthu, S. S., & Savalani, M. M. (n.d.). Handbook of sustainability in additive manufacturing (Vol. 2). Springer.
70. Klar, E., & Samal, P. K. (2007). Powder metallurgy stainless steels: processing, microstructures, and properties. ASM international.
71. Al-Mangour, B. (2015). Powder metallurgy of stainless steel: State-of-the art, challenges, and development.
72. Meng, J., Loh, N. H., Fu, G., Tor, S. B., & Tay, B. Y. (2010). Replication and characterization of 316L stainless steel micro-mixer by micro powder injection molding. Journal of Alloys and Compounds, 496(1–2), 293–299.
73. Handbook, A. S. M. (2005). Volume 1. Properties and Selection: Irons, Steels, and High Performance Alloys, 1
74. Mataya, M. C., Nilsson, E. R., Brown, E. L., & Krauss, G. (2003). Hot working and recrystallization of As-Cast 316L. Metallurgical and Materials Transactions A, 34(8), 1683–1703.
75. Hadi, M. (2019). Effect of powder characteristics on parts fabricated via binder jetting process. Rapid Prototyping Journal, 25(2), 332–342.
76. Rishmawi, I. (2019). Binder Jetting and Heat Treatment of Ferrous Alloys. University of Waterloo.
77. Dawes, J., Bowerman, R., & Trepleton, R. (2015). Introduction to the additive manufacturing powder metallurgy supply chain. Johnson Matthey Technology Review, 59(3), 243–256.
78. Anderson, I. E., White, E. M. H., & Dehoff, R. (2018). Feedstock powder processing research needs for additive manufacturing development. Current Opinion in Solid State and Materials Science, 22(1), 8–15.
79. Hausnerova, B., Mukund, B. N., & Sanetrnik, D. (2017). Rheological properties of gas and water atomized 17-4PH stainless steel MIM feedstocks: Effect of powder shape and size. Powder Technology, 312, 152–158.

80. Suri, P., Koseski, R. P., & German, R. M. (2005). Microstructural evolution of injection molded gas-and water-atomized 316L stainless steel powder during sintering. Materials Science and Engineering: A, 402(1–2), 341–348.
81. J. Zhao, M.P. Harmer, J. Am. Ceram. Soc. 71 (1988) 113–120.
82. Coe, H. G., & Pasebani, S. (2020). Use of Bimodal Particle Size Distribution in Selective Laser Melting of 316L Stainless Steel. Journal of Manufacturing and Materials Processing, 4(1), 8.
83. Kuczynski, G. C. (1990). Model experiments and the theory of sintering. In Sintering Key Papers (pp. 501–508). Springer.
84. Zhang, R. (2005). Numerical simulation of solid-state sintering of metal powder compact dominated by grain boundary diffusion.
85. Y.I. Frenkel. Viscous flow of crystalline bodies under the action of surface tension. Journal of Physics, 9(5):385{391, 1945.
86. Shaler, A. J., & Wulff, J. (1948). Mechanism of sintering. Industrial & Engineering Chemistry, 40(5), 838–842.
87. G.C. Kuczynski. Self-diffusion in sintering of metallic particles. Journal of Metals, 1(2):169{178, 1949.
88. German, R. M. (2010). Coarsening in sintering: grain shape distribution, grain size distribution, and grain growth kinetics in solid-pore systems. Critical Reviews in Solid State and Materials Sciences, 35(4), 263–305.
89. J.G.R. Rockland. The Determination of the Mechanism of Sintering. Acta Metallurgica, 15(1), 1967.
90. Blaine, D. C., Park, S. J., German, R. M., & Suri, P. (2006). Application of work-of-sintering concepts in powder metals. Metallurgical and Materials Transactions A, 37(9), 2827–2835.
91. R.M. German, P. Suri, and S.J. Park. Review: Liquid phase sintering. Journal of Materials Science, 44(1):1{39, 2009
92. R.M. German. Supersolidus Liquid Phase Sintering Part I: Process Review. Inter-national Journal of Powder Metallurgy, 26(1), 1990.
93. Gutmanas, E. Y. (1980). High-pressure compaction and cold sintering of stainless steel powders. Powder Metallurgy International, 12(4), 178–183.

94. Min, W., xing, A., & jun, Z. (2014). The effect of sintering additives on ceramic material sintering densification process based on cellular automata model. Computational Materials Science, 90, 16–22.
95. German, R. M. (1996). Sintering theory and practice. Solar-Terrestrial Physics, 568.
96. Hansen, J. D., Rusin, R. P., Teng, M., & Johnson, D. L. (1992). Combined-Stage Sintering Model. Journal of the American Ceramic Society, 75(5), 1129–1135.
97. Su, H., & Johnson, D. L. (1996). Master sintering curve: a practical approach to sintering. Journal of the American Ceramic Society, 79(12), 3211–3217.
98. Teng, M.-H., Lai, Y.-C., & Chen, Y.-T. (2002). A computer program of master sintering curve model to accurately predict sintering results. Western Pacific Earth Sciences, 2(2), 171–180.
99. Lee, Y.-S., Lee, S.-J., Lee, S., Kim, E.-Z., & Yoon, D. J. (2016). Development of a Master Sintering Curve for Al-Mg Alloy. Advances in Materials Science and Engineering, 2016.
100. Levasseur, D., & Brochu, M. (2016). Effect of heating rate on the pressureless sintering densification of a nickel-based superalloy. Metallurgical and Materials Transactions A, 47(5), 2257–2266.
101. www.retsch-technology.com
102. www.freemantech.co.uk
103. www.mtixtl.com
104. Lee, J. H., & Kim, Y. (2015). Intergranular Corrosion of 316L Stainless Steel by Aging and UNSM (Ultrasonic Nano-crystal Surface Modification) treatment. Corrosion Science and Technology, 14, 313–324.
105. Defay, R., & Prigogine, I. (1951). Tension superficielle et adsorption, 295 pp. Desser, Liege, Belgium.
106. www.netzsch-thermal-analysis.com
107. www.quantachrome.com
108. ASTM (2008) ASTM B962 - 17 Standard test methods for density of compacted or sintered powder metallurgy (PM) products using Archimedes' principle, ASTM B962 - 17 Stand. test methods density compact. or sintered powder Metall Prod Using Arch Princ.

109. Natarajan, A., Kelkar, R. M., Schoonover, J. J., Singh, P., Venkataramani, V. S., Chan, K. P., & Leman, J. (2018, March 15). Reversible binders for use in binder jetting additive manufacturing techniques. Google Patents.
110. T.-Y. Chan, M.-S. Chuang, S.-T. Lin, Injection moulding of oxide reduced copper powders, Powder Metall. 48 (2005) 129–133.
111. L. Moballegh, J. Morshedian, M. Esfandeh, Copper injection molding using a thermoplastic binder based on paraffin wax, Mater. Lett. 59 (2005) 2832–2837.
112. M.J. Donachie, S.J. Donachie, Superalloys: a technical guide, ASM international, 2002.
113. V. Ganesan, V. Seetharaman, V.S. Raghunathan, Interdiffusion in the type 316 austenitic stainless steel/iron system, J. Nucl. Mater. 118 (1983) 313–319.
114. M. Mizouchi, Y. Yamazaki, Y. Iijima, K. Arioka, Low temperature grain boundary diffusion of chromium in SUS316 and 316L stainless steels, Mater. Trans. 45 (2004) 2945–2950.
115. Z.Y. Liu, N.H. Loh, K.A. Khor, S.B. Tor, Sintering activation energy of powder injection molded 316L stainless steel, Scr. Mater. 44 (2001) 1131–1137.
116. Y. Wu, R.M. German, D. Blaine, B. Marx, C. Schlaefer, Effects of residual carbon content on sintering shrinkage, microstructure and mechanical properties of injection molded 17-4 PH stainless steel, J. Mater. Sci. 37 (2002) 3573–3583.
117. C.-C. Hsieh, W. Wu, Overview of intermetallic sigma (?) phase precipitation in stainless steels, Isrn Metall. 2012 (2012).
118. P.E. Evans, D.W. Ashall, Grain growth in sintered nickel powder, Int. J. Powder Met. 1 (1965) 32.
119. Z.Z. Fang, Sintering of advanced materials, Elsevier, 2010.
120. A.B. Spierings, M. Voegtlin, T. Bauer, K. Wegener, Powder flowability characterisation methodology for powder-bed-based metal additive manufacturing, Prog. Addit. Manuf. 1 (2016) 9–20.
121. A. Perron, C. Toffolon-Masclet, X. Ledoux, F. Buy, T. Guilbert, S. Urvoy, S. Bosonnet, B. Marini, F. Cortial, G. Texier, Understanding sigma-phase precipitation in a stabilized austenitic stainless steel (316Nb) through complementary CALPHAD-based and experimental investigations, Acta Mater. 79 (2014) 16–29.

122. B. Verlee, T. Dormal, J. Lecomte-Beckers, Density and porosity control of sintered 316l stainless steel parts produced by additive manufacturing, Powder Metall. 55 (2012) 260–267. https://doi.org/10.1179/0032589912Z.00000000082.